PMM/A-117

COMISION NACIONAL DE ENERGIA ATOMICA
DEPENDIENTE DE LA PRESIDENCIA DE LA NACION

OCTAVO CURSO PANAMERICANO DE METALURGIA

FABRICACION Y PROPIEDADES DE VAINAS DE ZIRCALOY

(Algunos Temas)

Krister Källström
Martin Svenzon

Departamento de Metalurgia
Buenos Aires - Argentina

1972

PMM/A-117

COMISION NACIONAL DE ENERGIA ATOMICA
DEPENDIENTE DE LA PRESIDENCIA DE LA NACION

OCTAVO CURSO PANAMERICANO DE METALURGIA

FABRICACION Y PROPIEDADES DE VAINAS DE ZIRCALOY

(Algunos Temas)

Krister Källström
Martin Svenzon

Departamento de Metalurgia
Buenos Aires - Argentina

1972

Sandvik · Sandviken · Sweden

by Mr. B. Larsson, Sandvik, Sandviken, Sweden

ABSTRACT

Quality requirements on canning tubes for nuclear service are probably the most exacting which a tube producer may encounter today. A satisfactory quality level must be based on a carefully selected production sequence and a well--established quality control and assurance system. The lecture presents a survey of the normally used manufacturing methods from raw material in the form of sponge to finished canning tubes. The influence of production parameters on the properties of Zircaloy canning tubes is discussed and the methods of non-destructive and destructive testing are reviewed. The paper mainly deals with Zircaloy. However, most of what is said can also be applied to stainless steel.

INTRODUCTION

The demands on the integrity of the canning tubes in a thermal reactor are very high. The reasons for this are obvious. Leakage in the fuel elements may lead to serious disturbances in the operation of the reactor and the economic loss connected with a shutdown is very high.

Fig. 1 is a summary of requirements on the canning tubes with regard both to the manufacture of fuel elements and to their use in the reactor. As can be seen, some of these requirements appear in more than one place, e.g. low impurity levels in the material, good dimensional accuracy and cleanness. Very important for the use is of course freedom from defects and the combination of strength and ductility of the canning material.

In the following an attempt will be made to present the ways of fulfilling the demands in canning tube production. Aspects on production sequences and on facilities used in production, inspection and quality control are the main topics. The survey will in the first place deal with Zircaloy tubing but since the production routes and the equipment used in most cases are the same, most of what is said about Zircaloy is applicable also to stainless steel.

MANUFACTURE OF ZIRCALOY

The main operations in the production of canning tubes in Zircaloy from sponge are shown in the block diagram in Fig. 2. To be able to meet the specified analysis on the ingot, we must have sponge with very low contents of impurities, especially of those with high cross section for thermal neutrons, for instance Hf.

Uniformity in analysis within the sponge lots is also important. The alloying elements of which oxygen is an important one are added to the sponge.

The pressed briquettes are electron beam welded to form an electrode which is melted in a high-vacuum arc furnace at a pressure of about 10^{-3} mm Hg. This operation is done twice to ensure uniformity and homogeneity in the final ingot.

Zirconium has a hexagonal lattice at room temperature. In pure Zr this α-phase is stable up to 862°C where it transforms to the face-centered cubic β-Zr. In the commercial alloys this transformation takes place over a temperature range where the material contains $\alpha + \beta$, Fig. 3.

Forging of Zircaloy is done in the $\alpha + \beta$ or the β-region. The equipment can be quite conventional. However, one must be sure that the heating conditions are such that no harmful diffusion of gases into the material takes place. The atmosphere should be slightly oxidizing. During cooling of the ingot and also after forging a secondary phase rich in the alloying elements Sn, Cr, Fe (and Ni for Zircaloy 2) will precipitate (Fig. 3). If this precipitation is not uniformly distributed in the material, it will have a negative influence on the corrosion properties. Therefore a β-quench is performed, i.e. heating to the β-region (~1050°C) and quenching.

The extrusion billets are prepared by drilling and turning. They are normally clad with copper to protect against surface contamination during heating and also to facilitate the lubrication during extrusion. The copper is removed after extrusion by pickling in nitric acid.

Extrusion is done in the α-region, i.e. at a temperature lower than 825°C. The microstructure of an extruded Zircaloy tube is shown in Fig. 4.

Cold working of Zircaloy tubes is normally performed as pilgering. Cold drawing is not used, because of the pronounced tendency of zirconium to gall and seize in the die which makes it difficult to find suitable lubricants. Besides, drawing is considered to give an undesirable texture in the tube wall, which will be discussed later. Pilgering can be performed with area reductions up to 80%.

All annealing operations must be carried out in vacuum lower than 10^{-3} mm Hg to prevent contamination of gases. The temperature of the intermediate annealings is around 650-700°C. To meet different requirements on mechanical properties the final annealing temperature may vary between 475-575°C.

In all stages of the production process the surface quality of the tubes must be carefully controlled. Surface conditioning of the finished tubes may involve inside vacuum blasting and acid flushing and outside belt grinding and pickling. The aim of all surface conditioning of finished tubes is to give them a surface with favourable properties with regard to corrosion resistance after autoclave treatment. Low surface standard will lead to a grey or white oxide layer instead of the desired black homogeneous surface.

Vacuum blasting and belt grinding are normally done with SiC since the use of Al_2O_3 may lead to the undesirable formation of zirconium oxide according to the formula

$$3\ Zr + 2\ Al_2O_3 \longrightarrow 3\ ZrO_2 + 4\ Al$$

This is especially important if the mechanical surface treatment is not followed by any removal of material by pickling.

Pickling is done in a HF-HNO_3-bath where the HNO_3 to HF ratio is around 10:1. The HF content is normally 2-3%. The result of the pickling operation is very much affected by the time between the pickling and rinsing operations and also by the efficiency of the rinsing. Unsufficient rinsing may lead to white oxide spots due to fluoride residues on the surface.

MECHANICAL PROPERTIES OF ZIRCALOY CANNING TUBES

The mechanical properties of the canning tubes mainly depend on the following three variables:
texture,
area reduction in the final rolling,
final annealing temperature.

Cold working of tubes by pilgering or drawing gives the material a texture where the c-axes of the crystals, i.e. the basal poles, are oriented in a direction perpendicular to the longitudinal axis of the tube. The direction of the basal poles within that plane can be affected by changing the so-called Q-value. This value is defined as the ratio between the reduction in wall thickness and the reduction in diameter.

$$Q = \frac{t_0 - t_1}{t_0} \times \frac{D_0}{D_0 - D_1}$$

where
t_0 = wall thickness before cold working
t_1 = wall thickness after cold working
D_0 = average diameter before cold working
D_1 = average diameter after cold working

A high Q-value, i.e. heavy reduction of the wall and little reduction of the diameter, will lead to a texture where the basal poles are oriented mainly in the radial direction, while a low Q-value (which is normal in drawing) will lead to tangentially oriented crystals (Fig. 5).

In practice, variations in the Q-value are obtained by rolling on mandrels with different conicity. Since the c-direction is the "hard direction" in the crystal, rolling with a high Q-value gives a tube with high hardness in the radial direction and rolling with a low Q-value gives high hardness in the tangential direction.

When deciding the Q-value one also has to take the hydride orientation into consideration. Hydrogen is absorbed by the tube in service and precipitates during cooling in plate-like hydrides. These hydrides precipitate in the direction perpendicular to the main working direction in the last cold working operation. This means that cold working with a very high Q-value gives tangential hydrides and cold working with a very low Q-value gives radial hydrides. This is illustrated in Fig. 6. As the hydrides reduce ductility and may initiate cracks, the canning tube users normally specify a hydride orientation that must not differ too much from the tangential.

The other factors influencing the mechanical properties of the finished tubes were area reduction and final annealing temperature. Fig. 7 and 8 illustrate how yield strength and elongation are affected by these factors. For high area reductions the mechanical properties change very rapidly with annealing temperatures around 500°C. In some cases the requested mechanical properties necessitate annealing in this temperature range, giving a partially recrystallized material.

In such cases the exact annealing temperature must be determined individually for every lot of tubes. Furthermore, the temperature accuracy of the annealing furnace must be very good, better than ±3°C is necessary in some cases.

Very often transverse properties are specified. These are usually determined by burst testing with an inside overpressure. Burst testing can be done with open or closed ends (Fig. 9) and it is important to define which method shall be used. The closed-end testing gives a stress ratio of 2:1 between the tangential and axial direction. This method gives substantially lower values on transverse elongation than the open-end method which gives a uniaxial tangential stress in the tube.

STAINLESS STEEL CANNING TUBES

The English AGR is practically the only type of commercial thermal reactor using stainless steel for cladding. The material used is a niobium-stabilized 20Cr/25Ni austenitic steel. The production sequence for canning tubes in stainless steel is very similar to that given for Zircaloy. In order to get a very pure steel free from harmful inclusions, the steel is melted twice, first in an induction furnace with very pure raw materials and then remelted in the same type of furnace as is used for Zircaloy, the vacuum arc furnace.

Although the hot working temperatures differ, the methods used are the same. This also applies to cold working where, however, drawing is used more than for Zircaloy. Canning tubes in stainless steels are often delivered in the cold worked condition (area reduction of 15-25%) to give the tubes a higher initial yield point than what is possible to reach with the annealed condition.

QUALITY CONTROL

General

The high quality demands on canning tubes are reflected in the specified limits for dimensional tolerances and defects. Tolerances are specified either for ID and OD with a minimum wall thickness or for ID and wall thickness.

Normal tolerances are:	for ID	± 0.04 mm
	for OD	± 0.05 mm
	for wall thickness	± 10%

The demands on freedom from surface defects, cracks, etc. are very stringent. The rejection level is often very close to what is possible to detect with reliability with the most advanced testing methods and equipment.

It is not possible to make a high-quality product only by very accurate final inspection. The quality of the finished product is a function of the processes by which it is produced. In other words, proper processing methods and an extensive in-process control are necessary means to establish good quality.

In-process control

Besides the chemical composition, which is controlled on samples from the top, middle and bottom of every vacuum melted ingot, there are many factors to control. In the forged bar stage, an ultrasonic examination is normally performed to ensure that the material is free from internal defects. Furthermore, in the preparation of extrusion billets the centre part of the bar is removed by drilling. In the production sequence for canning tubes, intermediate inspections with control of dimensions, surfaces, etc. are frequent operations. However, the process control shall not only inspect the tubes after operations like extrusion, cold rolling, annealing, etc. It is preferable to make spot checks in the course of the operations so that possible discrepancies are found and adjusted at an early stage.

Final inspection

Before being shipped to the customer, the canning tubes pass an extensive final inspection where tolerances, freedom from defects, specified properties etc. are checked (Fig. 10). Defective tubes are sorted out and, if possible, reconditioned and rechecked. If that is not possible, they are scrapped.

The tolerances on the inner and outer diameter are relatively close and it is necessary to control the diameters along the entire length of every tube.

The measuring of diameters is done using air gauges or electro-mechanical gauges. The air gauge is unexpensive and accurate but slow and gives a mean value over a relatively large section of the circumference. The electro-mechanical gauge is more expensive but fast and very flexible. It also measures a more true diameter as it measures the distance between two points in contact with the tube surface and can register very local variations in diameter. The result of the test is normally recorded on a chart.

For the detection of material defects a 100% ultrasonic testing is specified by all customers. The calibration of sensitivity and rejection level is done against in- and outside standard defects for which form, length and depth are prescribed by the customer.

Normally the rejection level is set equal to the amplitude of the signal from the standard defect (100%) but 75 and 50% of this amplitude are sometimes specified as the rejection level. Simultaneous testing for longitudinal and transverse defects is always requested. The standard defects can be down to 1 mm in length and the depth is normally 10% of the tube wall. They are made either by machining with a special tool in a lathe, or by the electrical discharge method. The fact that the standard defects are so small may lead to disturbances from a tube not perfectly cleaned or from an uneven grain size in the material. The latter case is something which especially must be taken into account when stainless steel tubes are tested. The testing is made in four directions, with two transducers each for longitudinal and transverse defects (Fig. 11).

The tube surface is scanned along a helical line with a pitch determined by a demand for a certain degree of overlapping. The signals from defects are recorded. To check the calibration, a tube containing the standard defects is run through the test unit at constant intervals, e.g. once every half-hour.

The wall thickness of the tubes is normally checked simultaneously with the defect control since it is performed by means of an ultrasonic resonance method. Calibration of this equipment is done by means of minimum and maximum wall thickness samples according to the specified tolerance limits.

The normally required destructive tests are also listed in Fig. 10. Check analyses for oxygen, hydrogen and nitrogen are requested to establish that no harmful contamination has occurred during the manufacture. Tensile testing is performed both at room temperature and at elevated temperature, normally the operation or design temperature. The burst testing for circumferential elongation has already been dealt with in connection with the mechanical properties. A standard autoclave test is always performed. It takes place in steam at 400°C for 3 days, and afterwards the weight gain of the samples is measured.

The hydride orientation is normally determined after loading the samples with hydrogen to a content of 100-200 ppm. Hydride orientation is usually specified by the F_n-number, defined as the ratio between the number of radial hydrides and the total number of hydrides observed in a transverse section of the tube.

The results of all tests are compiled in a certificate for every lot of tubes. This certificate is sent with the material to the customer.

FINAL REMARKS

A considerable part of the costs for the finished tubes lies in inspection and control. This is a natural consequence of the very high demands on the material which necessitate the use of technically very advanced methods for testing and inspection as well as for production.

Of course, there is a mutual interest from the supplier and the user to keep the total costs of the product down as much as possible. The best way to achieve this is an intimate contact and cooperation in such specification questions as properties and tolerances but also concerning methods and the extent of control.

1. Requirements with regard to the manufacture of the fuel elements
   a) Dimensional accuracy (ID and OD)
   b) Adequate straightness
   c) Proper cleanness
2. Requirements with regard to the application
   a) Low cross section for thermal neutrons
      Analysis - low impurity level
      Thin wall
   b) Adequate strength and ductility, determined by
      Oxygen content
      Tensile strength and ductility
      Transverse ductility
      Hydride orientation
      Freedom from defects
      Dimensional accuracy (excentricity)
   c) Good corrosion resistance to the coolant
      Low impurity levels
      Favourable microstructure
      Adequate surface finish
      Proper cleanness (e.g. freedom from fluorides)

Fig. 1
Requirements on canning tubes

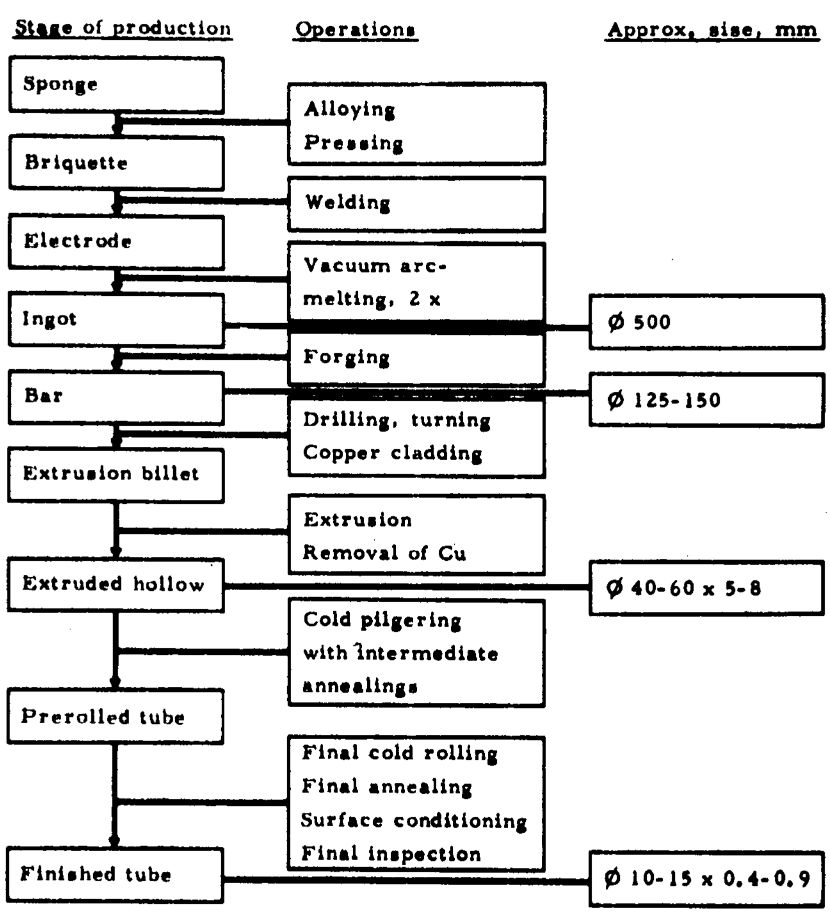

Fig. 2
Production sequence for Zircaloy canning tubes

TRANSFORMATION TEMPERATURES $\alpha \rightleftharpoons \beta$

Zirconium		862°C
Zircaloy-2	Heating	825-985°C
	Cooling	945-780°C

APPROX. COMPOSITION OF SECONDARY PHASE IN ZIRCALOY-2

Fe	Ni	Cr	Sn	Zr	
7	7	1	1.5	83.5	Weight-%

Fig. 3

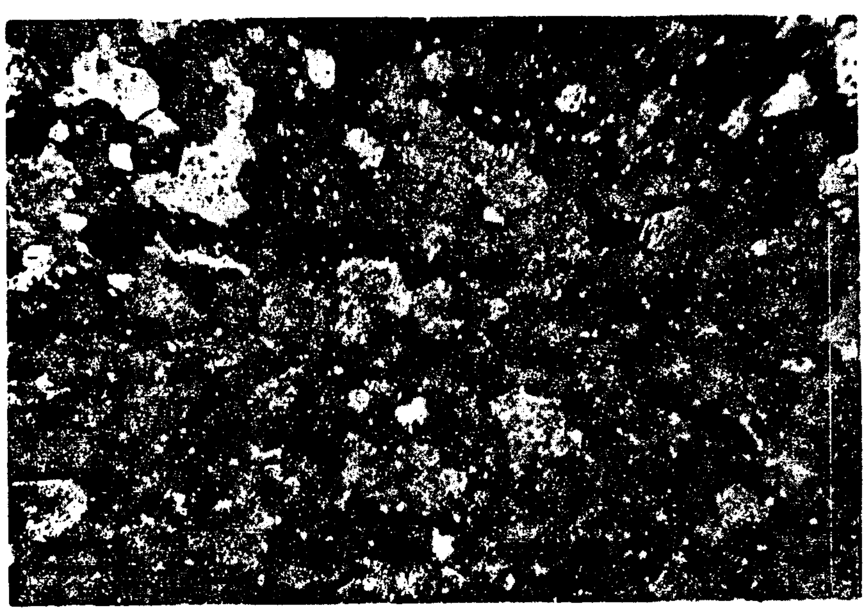

Fig. 4
Microstructure of extruded Zircaloy tube, transverse section. x 800

Texture after reduction of

diameter (low Q) wall thickness (high Q)

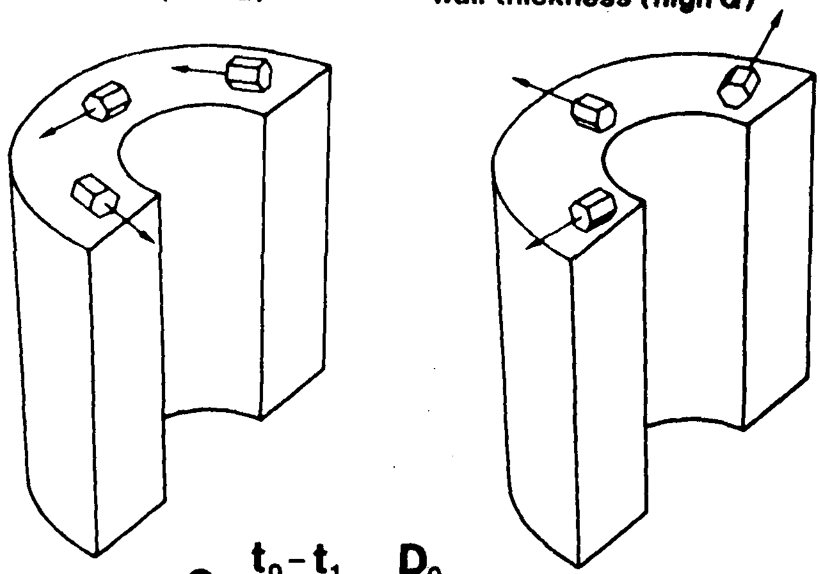

$$Q = \frac{t_0 - t_1}{t_1} \cdot \frac{D_0}{D_0 - D_1}$$

Fig. 5
Variation in texture with different Q-values

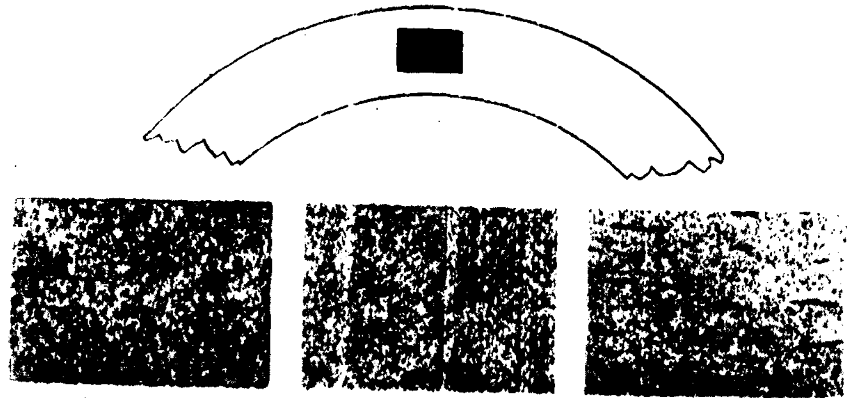

Fig. 6
Variation in hydride orientation with different Q-values

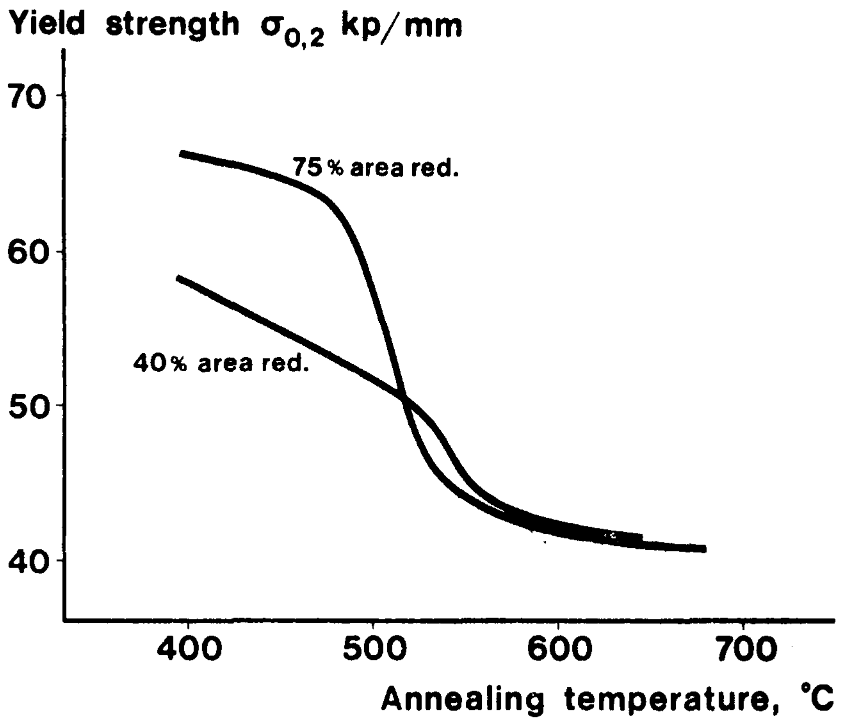

Fig. 7
Mechanical properties of Zircaloy as a function of annealing temperature and area reduction

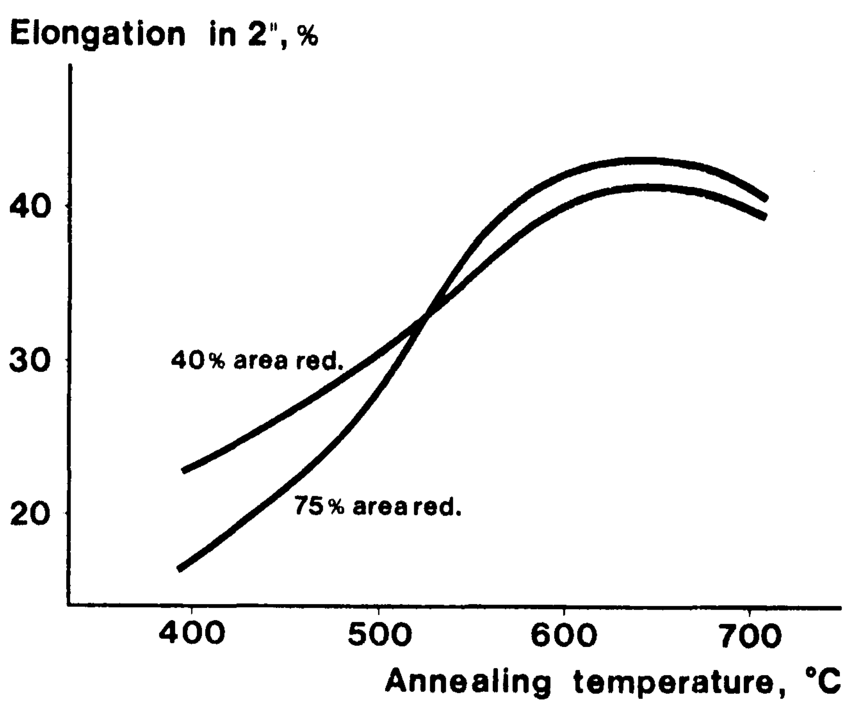

Fig. 8
Mechanical properties of Zircaloy as a function of annealing temperature and area reduction

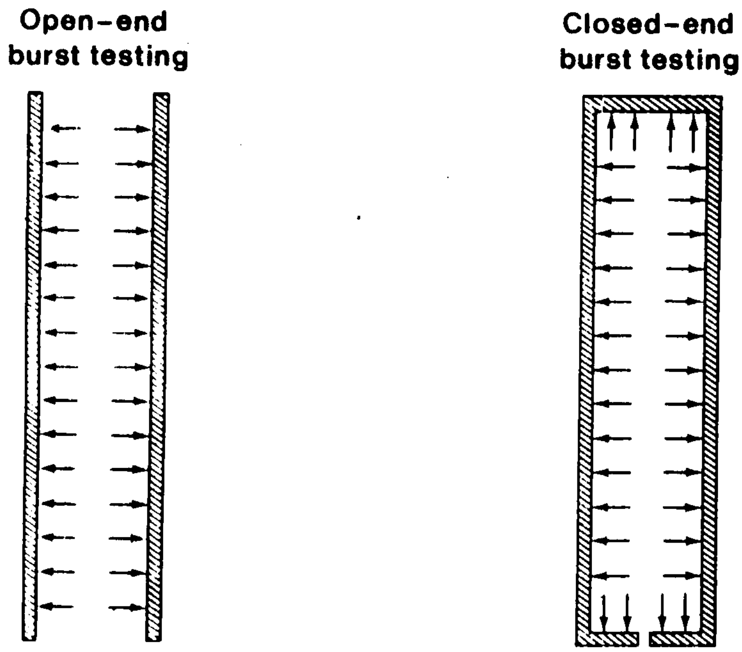

The internal pressure gives a tangential stress in the tube wall.

The internal pressure gives a tangential stress and an axial stress with the ratio 2:1 in the tube wall.

Fig. 9
Principles of open-end burst testing and closed-end burst testing

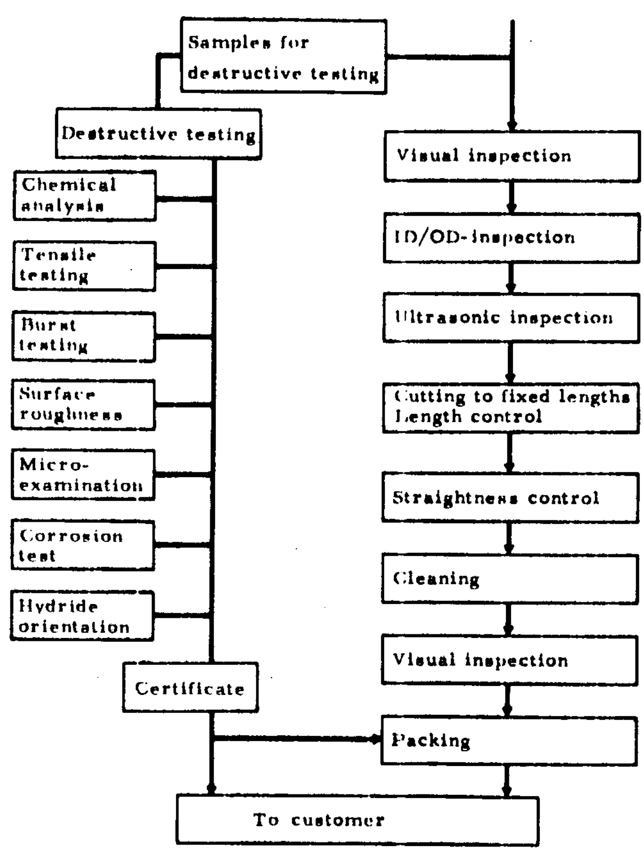

Fig. 10
Final inspection and testing of canning tubes

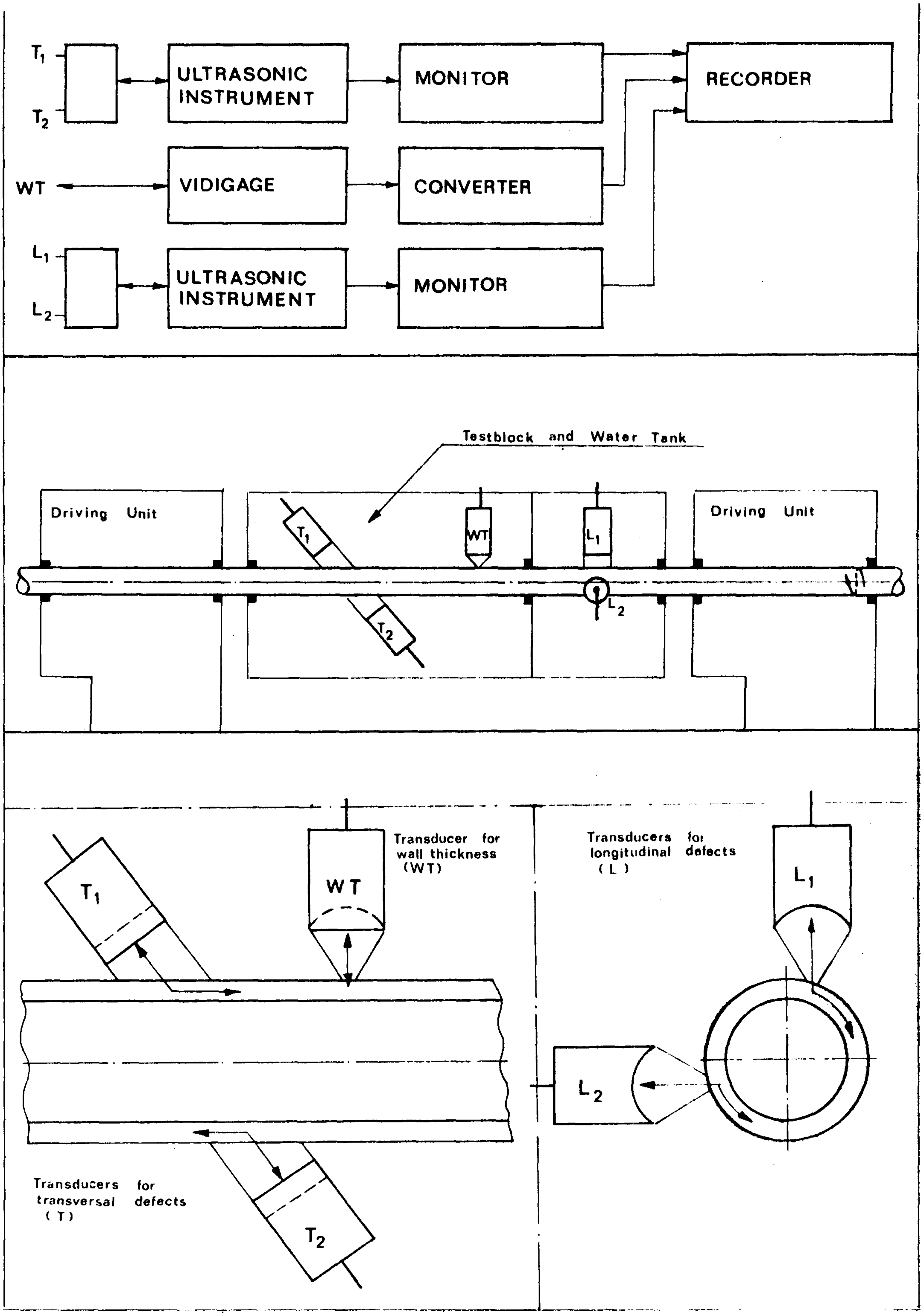

Fig. 11
Principle arrangement for ultrasonic inspection and wall thickness test of cladding tubes

Krister Källström

Texture and anisotropy of zirconium in relation to plastic deformation

Abstract. Possible modes of plastic deformation of tubular materials are analyzed generally. Based on symmetry considerations applied to known textures of zirconium wire and strip, textures of zirconium tubes are predicted as resulting from a wide range of deformation modes. This is made possible by focusing on the main feature of texture, i.e., the orientation distribution of basal poles. A relation between texture and the mechanical anisotropy of zirconium is developed, and rules are suggested for softening and hardening caused by texture change. Experimentally, Zircaloy tubes were deformed by various techniques. The resulting textures were determined by X-ray diffraction and the mechanical anisotropy by Knoop-hardness measurement. Each determination is condensed into two representative figures, one describing the type of texture or anisotropy and the other describing the sharpness of texture or the degree of deviation from isotropy.

The experiments verify the predicted relation between type of texture and mechanical anisotropy, and also indicate how degree of anisotropy depends on sharpness of texture. Changes in texture are investigated in relation to plastic deformation, and further refined rules are derived for the direction and rate of these changes. The initially predicted textures are concluded to be stable, i.e., they are reached only after a certain degree of deformation. Zircaloy tubes of three different textures were subjected to tensile testing, closed-end burst testing and open-end burst testing. The observed texture-softening phenomenon corroborates the rules suggested and is considered to commonly occur, as opposed to texture hardening, which requires special combinations of texture and testing method.

Résumé. Les différents modes de déformation plastique possibles dans les tubes ont été analysés d'une façon générale. En se basant sur des considérations de symétrie appliquées aux textures connues pour le zirconium en fil et en bandes, la texture des tubes de zirconium résultant de divers modes de déformation a été prédite. Ceci est possible si l'on tient surtout compte des principes de la texture, c'est à dire, la distribution des orientations des pôles de base. Une relation entre la texture et l'anisotropie du zirconium est développée, et des règles sont suggérées pour l'adoucissement et la consolidation dûs à un changement de texture. Dans les expériences, les tubes de zirconium ont été déformés par plusieurs modes. Les textures résultantes ont été déterminées par la diffraction des rayons-X, et l'anisotropie par des mesures de dureté Knoop. Chacune de ces déterminations est représentée dans deux figures, l'une décrivant le genre de texture ou anisotropie, l'autre décrivant la netteté de la texture ou l'écart du caractère isotrope. Les expériences vérifient la relation prévue entre la texture et l'anisotropie. Les changements de texture sont examinés en fonction de la déformation plastique, et d'autres règles plus rigoureuses sont dérivées pour la direction et la vitesse de ces changements. On conclut que les textures prévues initialement sont stables, c'est à dire qu'elles ont lieu après une certaine déformation. Des tubes de Zircalloy de trois textures différentes ont été soumis à des essais de traction, des essais d'éclatement à extrémités ouvertes ou fermées.

Le phénomène d'adoucissement observé, causé par la texture, est en accord avec les règles suggérées et est généralement présent, ce qui n'est pas le cas du durcissement causé par la texture, durcissement nécessitant des combinaisons spéciales de texture et de méthodes d'essai.

The hexagonal close-packed (hcp) metal zirconium has a crystal lattice with a unique direction, the basal plane normal or basal pole [0001], implying a pronounced anisotropy. This results in plastic deformation that occurs either by slip or twinning. The slip systems are of the type $\{10\bar{1}0\}$ $\langle 1\bar{2}10\rangle$ with all slip directions perpendicular to the [0001]. Thus tension or compression along [0001] can not be accommodated by slip. Instead, twinning occurs and this requires a higher resolved shear stress than slip, making [0001] a strong direction of the crystal. The anisotropy of zirconium single crystals is present in the polycrystalline metal, which normally is heavily textured and has anisotropic properties. This is of special importance to the mechanical properties of Zircaloy tubes in their use as fuel sheathing in nuclear reactors (Table I). In Zircaloy the hcp alpha phase is dominant, giving Zircaloy the same characteristics as regards texture and anisotropy as pure zirconium. In the following, the word zirconium should be

Table I. Alloying elements in Zircaloy-2 and Zircaloy-4, weight per cent

	Sn	Fe	Cr	Ni	O
Zircaloy-2	1.5	0.13	0.10	0.05	0.12
Zircaloy-4	1.5	0.20	0.10	–	0.12

Krister Källström is with The Sandvik Steel Works, Sandviken, Sweden.

interpreted as including Zircaloy as well as other dilute alloys where the alpha phase is dominant.

Zirconium textures in wire and strip have been recorded and reported (1,2) and also thoroughly reviewed (3). A number of investigations (4-9) have illustrated the effect of the basal pole orientation on such mechanical properties as yield strength, strain ratio and ductility in tensile and burst testing. An excellent study of how the texture of tubes is related to the preceding deformation and heat treatment has been reported by Cheadle, *et al.* (10), who concluded that the basal poles have a tendency to align themselves parallel to the direction of maximum compressive strain. Hobson (11) and Tenckhoff and Rittenhouse (12) found the texture of Zircaloy tubes to be a function of the Q-value of the deformation, i.e., the ratio between the reduction of wall thickness and the reduction of diameter. However, these studies do not answer the important question of what degree of deformation is required to bring about a change in texture. Also, the use of Q-values has restricted the range of deformation to reduction in both wall and diameter. It was felt that much would be gained by a more general approach, where the main features of texture and anisotropy are related to both the mode and degree of deformation.

The main features of texture are very important and these should be mapped before the details are worth considering. It is usually only the texture that influences the measurable anisotropy of the material. The main features may be regarded as a first-order effect and are a direct consequence of the basal pole orientation, whereas the rotation of crystals around the basal pole contributes to effects of higher order.

For texture and anisotropy studies, material in tubular form allows one more degree of freedom than wire drawing or strip rolling in selecting the mode of deformation, because arbitrary changes in both diameter and wall thickness are possible. In this work, the principal strain and stress directions during deformation are parallel to the principal directions of the tube, i.e., the radial, the tangential and the axial direction, denoted r, Θ, z. Being parallel makes all anisotropic properties, including the texture, symmetric with respect to the three principal directions of the tube.

Texture of zirconium. The textures from wire drawing, compression of cylinders and strip rolling are characterized in a simple way in Table II, both after deformation and after subsequent recrystallization (1-3). Pole figures provide a detailed description of textures and since only the basal pole orientation is of interest here, only basal pole figures are relevant. In Figure 1 typical basal pole figures are given for drawing, compression and rolling where the drawing axis is 3, the compression axis 1, the rolling plane normal 1 and the rolling direction 3. The rolling deformation process gives elongation and thinning usually with constant width.

Table II. Textures in Zirconium

	Drawing Texture	Compression Texture	Rolling Texture
Deformation texture	$\langle 10\bar{1}0\rangle$	$[0001]$	$(0001)\langle 10\bar{1}0\rangle$
Recrystallization texture	$\langle 11\bar{2}0\rangle$	$[0001]$	$(0001)\langle 11\bar{2}0\rangle$

This might be regarded as the sum of a longitudinal drawing and a compression in the normal direction, so that the narrowing from the drawing is compensated by the broadening from the compression. Therefore, the rolling texture is, at least approximately, the sum or the average of a drawing texture and a perpendicular compression texture.

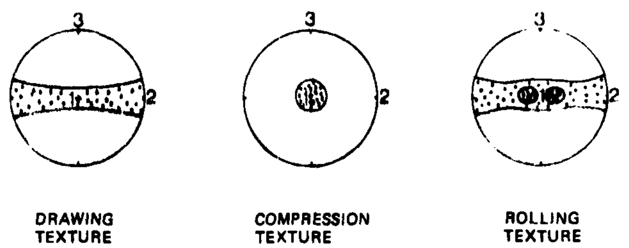

Figure 1. Typical basal pole figures of drawing texture, compression texture and rolling texture.

During recrystallization the crystals rotate 30° around [0001], which means the basal pole texture is essentially unaffected (3). Thus, the basal pole figures in Figure 1 are valid for recrystallization textures as well as deformation textures and the following discussion of texture and anisotropy is independent of whether recrystallization has occurred or not. The duplex appearance of the rolling texture in Figure 1 is characteristic for highly reduced zirconium strip. However, in the following discussion only the main features of the texture will be considered, as shown in Figure 2.

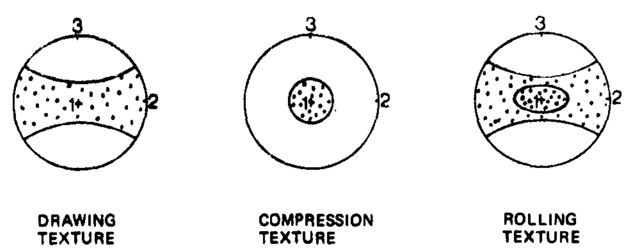

Figure 2. Basal pole figures of less pronounced or more approximate textures.

Symmetry considerations

Plastic deformation characterization. The principal strain directions are parallel to the principal tube directions only if an entire tube is considered before and after deformation, and there has been no torsion. During deformation the tube is-conical, suggesting shear strains and loss of parallelism, but those strains are relatively small and disappear when the tube resumes its cylindrical shape. It is justified to assume that parallelism exists, because the approximation introduces no significant errors, and because the analysis is simpler. When a rectangular parallelepiped with the dimensions t_0, w_0, l_0, is deformed plastically with the principal strain directions parallel to the edges, it will stay a rectangular parallelepiped after the deformation but with the new dimensions t, w, l. At constant volume

$$\ln\frac{t}{t_0} + \ln\frac{w}{w_0} + \ln\frac{l}{l_0} = 0 \qquad 1$$

The edges t, w, l are the wall thickness, the circumference and the length respectively, of a thin-walled tube, and the logarithmic strains ϵ_r, ϵ_Θ, ϵ_z give

$$\epsilon_r = \ln\frac{t}{t_0},\ \epsilon_\Theta = \ln\frac{\pi d}{\pi d_0} = \ln\frac{d}{d_0},\ \epsilon_z = \ln\frac{l}{l_0} \qquad 2$$

where d is the mean diameter. Substituting into Equation 1 gives

$$\epsilon_r + \epsilon_\Theta + \epsilon_z = 0 \qquad 3$$

This means a deformation is defined by only two independent variables and a function of two variables can be drawn on a plane diagram. To emphasize the equivalence of the principal directions a triaxial plane 120° diagram is chosen, and in the following referred to as the strain diagram (Figure 3).

Any change in the dimensions of a tube is represented by a vector in the strain diagram. The size and angle of the strain vector correspond directly to the degree and to the mode of deformation. The *effective strain* ϵ_e and the *strain ratio* α are introduced (13,14)

$$\epsilon_e = \sqrt{\frac{2}{3}\left(\epsilon_r^2 + \epsilon_\Theta^2 + \epsilon_z^2\right)} \qquad 4$$

$$\alpha = \arctan\left[(\epsilon_\Theta - \epsilon_r)/\epsilon_z\sqrt{3}\right] \qquad 5$$

The strain ratio is expressed as an angle α clockwise from the positive ϵ_z-axis to the direction of the strain vector (Figure 3). This ratio is defined as an angle to underline the equivalence of all α-values from $-180°$ to $+180°$. The generality of the definition of α is shown by the fact that, as the previously mentioned Q-value goes from 0 to 1 to ∞, α goes from $-30°$ to $0°$ to $+30°$.

A strain vector can be translated parallel in the strain diagram without changing its significance and vectors can be summed up to represent a series of deformation steps. Also, a deformation can be divided into a series of very small vectors, which together define a curve in the strain

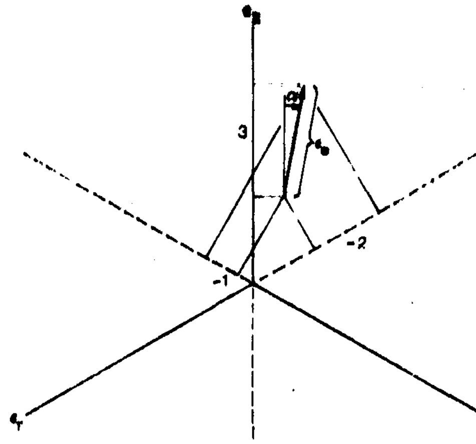

Figure 3. Plane triaxial strain diagram with strain vector, defined either by its strain components or by the effective strain ϵ_e and the strain ratio α.

diagram. Such a curve will be referred to as a *strain path.* According to the theory of plasticity, the above formulae should be based on infinitesimal strain elements $d\epsilon_i$, the effective strain should be an integral and a strain ratio should be valued at only one stage during the deformation (13,14). However, for practical purposes the given finite formulae are justified if used with care. To further illustrate the use of the strain ratio α, the deformation of tubes with $\alpha = n \cdot 30°$ is described in Table III.

Table III. Types of deformation corresponding to the specific strain ratios $\alpha = n \cdot 30°$

Strain Ratio	Deformation of Tubes as Defined by Changes in Wall Thickness, Diameter, and Length
$\alpha = 0°$	Elongation with equal wall thinning and diameter contraction
$\alpha = 30°$	Elongation with constant diameter
$\alpha = 60°$	Wall thinning with equal expansion and elongation
$\alpha = 90°$	Expansion with constant length
$\alpha = 120°$	Expansion with equal shortening and wall thinning
$\alpha = 150°$	Expansion with constant wall thickness
$\alpha = 180°$	Shortening with equal wall thickening and expansion
$\alpha = -150°$	Shortening with constant diameter
$\alpha = -120°$	Wall thickening with equal diameter contraction and shortening
$\alpha = -90°$	Diameter contraction with constant length
$\alpha = -60°$	Diameter contraction with equal elongation and wall thickening
$\alpha = -30°$	Elongation with constant wall thickness

The texture rose. The drawing texture is typical of wire, which can only be deformed through elongation with rotational symmetric contraction. The corresponding deformation of tubes is elongation with equal thinning of wall and diameter contraction, which gives the strain ratio $\alpha = 0°$. The compression texture is a result of shortening a cylinder with rotational symmetric expansion. One corresponding deformation of tubes is thinning of wall with equal diameter expansion and elongation, which gives the strain ratio $\alpha = 60°$. The two rotational symmetric pole figures from Figure 2 are accordingly inserted in a strain diagram at the direction of strain ratio 0 and 60° (Figure 4). The rolling texture is obtained from elongation with constant width. The corresponding deformation of tubes is elongation with constant diameter, which is the strain ratio $\alpha = 30°$. The rolling texture pole figure from Figure 2 is inserted at the strain ratio 30° in Figure 4.

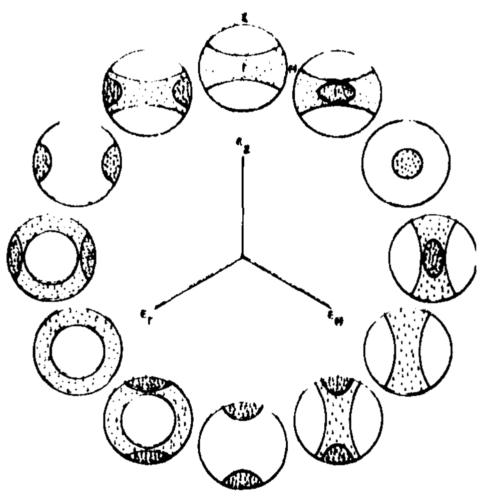

Figure 4. The texture rose relating the strain ratio to the resulting stable texture.

Rotational symmetric deformation is equivalent whether the symmetry axis is radial, tangential or axial, as is reflected by the threefold strain diagram. Thus, it is possible to introduce fibre textures at all the axes of the strain diagram both in their positive and negative directions, by permuting the texture axis of the pole figures (Figure 4). The rolling texture at $\alpha = 30°$ is the average of the two neighbouring fibre textures; similarly, there must be average textures between all the fibre textures in Figure 4. Thus, the strain diagram, although complete with twelve pole figures, should be regarded as representing a continuous ring of textures which are weighted averages of the surrounding fibre textures. The strain diagram completed with pole figures is referred to as the *texture rose* and expresses a general relationship between the mode of deformation of zirconium tubes and the resulting texture.

However, the relation between deformation and texture as given by the texture rose is expected to be valid only for stable textures, which require either a texture-free starting material or such a high degree of deformation that stability is reached. To handle unstable textures, the strain diagram in the centre of the rose is removed and a new parameter introduced. The *texture ratio* is an angle η measured clockwise from the rising vertical line through the centre of the texture rose, to the position of any recorded texture in the rose. For stable textures $\alpha = \eta$, while for unstable textures $\alpha \neq \eta$.

Yield locus and mechanical anisotropy. Yield loci are presented as projected on the deviator stress plane, containing the deviator stresses σ_r', σ_θ', σ_z' (13,14). This maintains the triaxial 120° symmetry as for the stress diagram, and makes the von Mises yield locus of an isotropic material circular. The yield locus in its first-order deviation from the circular form should be an ellipse. A fibre texture must have a yield locus symmetric to the same axis as the texture. In Figure 5(*a*) a compression texture with a radial axis is shown. Radial basal poles make the radial direction strong, and the corresponding yield locus consequently has its major axis along the σ_r'-axis. In Figure 5(*b*) a drawing texture with an axial axis is shown. Here the axial direction is weak, because the basal poles are perpendicular to this direction and the corresponding yield locus has its minor axis along the σ_z'-axis. The eccentricity of the ellipse in Figure 5(*a*) has been made greater than that in Figure 5(*b*) in order to show that basal poles parallel to a direction mean a greater anisotropy than basal poles oriented perpendicular to a direction. As the rolling texture is an average of the drawing and compression textures, the rolling-texture yield locus could be assumed to be an average of the drawing and compression texture yield loci (Figure 5(*c*)).

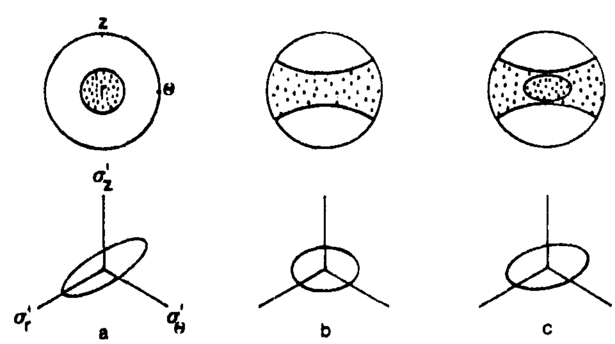

Figure 5. Yield loci corresponding to compression, drawing and rolling textures.

Therefore, it is possible to replace every pole figure in the texture rose with a schematic yield locus, by applying a simple symmetry consideration (Figure 6). If the direction of the major axis of the yield locus is the angle β, as shown in Figure 6, the following formula relates the strain ratio α to the orientation of the yield locus

$$\alpha = 2(90 - \beta) \qquad 6$$

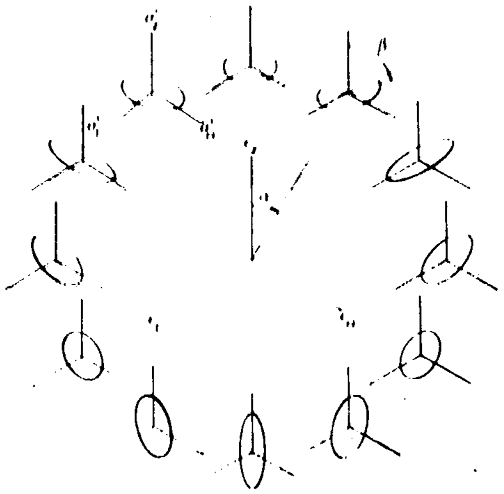

Figure 6. Relationship between the strain ratio and the resulting stable anisotropy as displayed by yield loci.

Again, this relation is valid only for stable textures and yield loci. To handle unstable yield loci it is convenient to introduce a new parameter, *anisotropy ratio* ν, where $\nu = 2(90 - \beta)$ is a function of the type of mechanical anisotropy. Consequently ν should be equal to η for all textures, while $\nu = \alpha$ only for stable textures. These statements are to be verified in the experiments.

Texture softening and hardening. Plastic deformation is forced upon the material by the forming process. In mechanical testing, on the other hand, the material is loaded under a given stress ratio. With the requisite of parallelism between the principal stress directions and the principal tube directions, a state of stress in the deviator stress diagram is given by a point, or by a stress vector from the origin to that point. The size of the stress vector is proportional to the *effective stress* σ_e and its angle corresponds to the *stress ratio* γ (13,14).

$$\sigma_e = \sqrt{\frac{1}{2}\left[(\sigma_1 - \sigma_2)^2 + (\sigma_2 - \sigma_3)^2 + (\sigma_3 - \sigma_1)^2\right]} \qquad 7$$

$$\gamma = \arctan\left[(\sigma_2 - \sigma_1)\sqrt{3}/(2\sigma_3 - \sigma_1 - \sigma_2)\right] \qquad 8$$

Like the strain ratio α, the stress ratio γ is expressed as an angle measured clockwise from the positive σ_z'-axis in the deviator stress diagram. Strain ratios of specific interest are $\gamma = 0°$ in tensile testing, $\gamma = 90°$ in closed-end burst testing and $\gamma = 120°$ in open-end burst testing.

On loading a tube with a given stress ratio until plastic deformation occurs, the strain ratio will be a function of both the stress ratio and the type of anisotropy. A rule is that the strain vector is perpendicular to the yield locus at the point where the yield locus is reached by the stress vector, if a combined strain-stress diagram is used (14). For

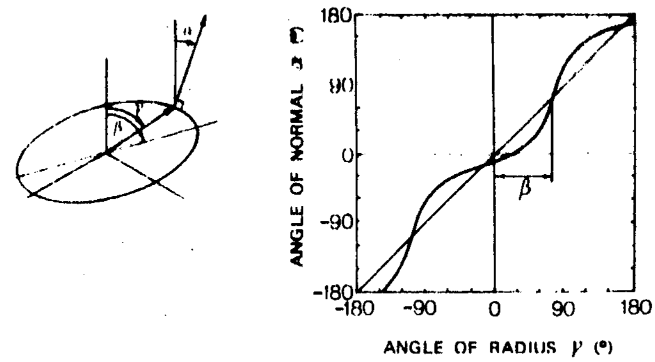

Figure 7. Relationship between the radius and the normal in a point on an ellipse.

an isotropic material the rule is normal, but it is also said to be valid for an anisotropic material (13). The pure geometric relation between the angle γ of the radius to a point on an ellipse and the angle α of the normal to the periphery at the same point is given as a periodic curve in Figure 7. By changing the orientation β of the major axis of the ellipse the curve is translated parallel to the $\alpha = \gamma$ -line. The periodic curve of Figure 7 can be assumed to show the relationship between the stress and strain ratios during mechanical testing. The periodicity 180° implies that

$$\alpha = \gamma \text{ when } \alpha = \beta + n \cdot 90 \qquad 9$$

where n stands for any positive or negative integer. The question here is if the strain during testing will bring about a change in texture and anisotropy or if the texture is stable for the strain. The relation between the strain ratio, the stable anisotropy ratio and the orientation of the major axis of the yield locus is, as previously stated, $\alpha = \nu = 2(90 - \beta)$ (Equation 6). Replacing α in Equation 9 gives

$$\nu = \gamma \text{ when } 2(90 - \beta) = \beta + n \cdot 90 \qquad 10$$

or after transformation

$$\nu = \gamma \text{ when } \nu = n \cdot 60 \qquad 11$$

Thus the relation between the stable anisotropy ratio and the stress ratio must be as shown in Figure 8 which is similar to Figure 7, but with the smaller periodicity of 120°.

If the anisotropy ratio is not stable for deformation under a given stress ratio, the texture will change so as to bring the anisotropy ratio towards its stable value. In this process either a softening or a hardening due to the texture change is anticipated, superimposed on the normal strain hardening. *Texture softening* is foreseen when the angle between the stress vector and the minor axis of the yield locus is greater at start, than when stable anisotropy is reached. *Texture hardening*, on the other hand, is foreseen when the angle between the stress vector and the major axis of the yield locus is greater at start, than when stable

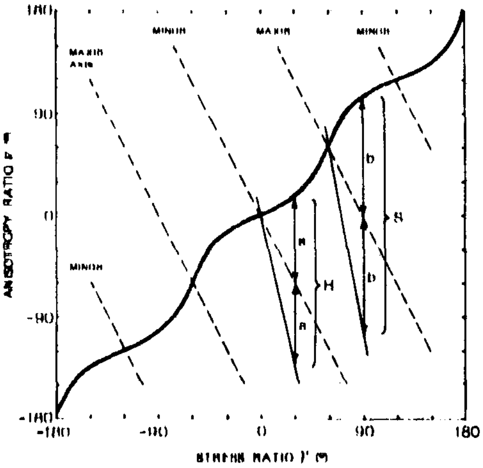

Figure 8. Periodic relationship between the stress ratio and the stable anisotropy ratio. Principle of construction of softening and hardening regions.

anisotropy is reached. To illustrate this, parallel dashed lines with the slope -2 are drawn in Figure 8, indicating those anisotropy ratios for which the major and the minor axes of the yield locus are parallel to the stress vector. Examples for $\gamma = 30°$ and $90°$ are given in Figure 8, where the range for hardening H is defined by the two equal distances marked a, and where the range for softening S is defined by the two equal distances marked b. In this way it is possible to divide the entire anisotropy ratio - stress ratio diagram into regions alternately giving texture softening S and texture hardening H (Figure 9). The region boundary curves are approximately straight lines with a slope of -5.

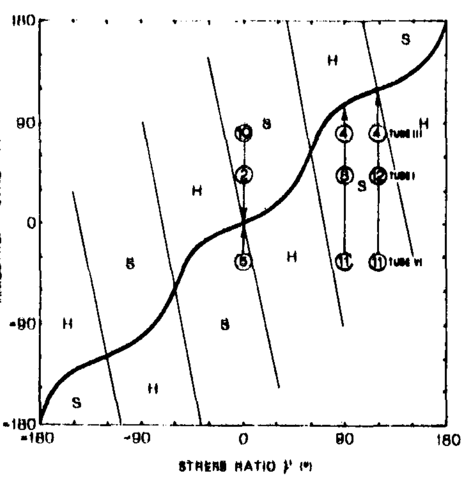

Figure 9. Anisotropy ratio-stress ratio diagram divided into regions for texture softening S and hardening H.

Experimental

Deformation experiments and mechanical testing. Tubes of Zircaloy-2 were deformed by six widely different methods, referred to as numbers I to VI and the ranges of strain ratios obtained are summarized in Table IV. In each experiment, specimens were taken from the starting material and at several stages during the deformation. The specimens were numbered in sequence as shown in Table IV. The starting material was normally recrystallized, but in one case, specimen 40, it was stress-relieved. Strain paths on the strain diagram show the results of the deformation experiments in more detail. To simplify, the triaxial strain diagram has been modified by introducing logarithmic scales for wall thickness and mean diameter on the ϵ_r- and ϵ_θ-axes, respectively (see Figures 10 and 11), where the strain paths are obtained directly by plotting wall thickness versus mean diameter.

Table IV. Deformation experiments with Zircaloy tubes

Deformation Technique	I	II	III	IV	V	VI
Range of Strain Ratio	20-27°	115-137°	120-145°	-145- -139°	84- 56°	35- 31°
Specimen Series No.	10-15	20-22	30-32 40-44 50-55	60-68	70-72	80-85

Tubes of Zircaloy-4 were selected for mechanical testing. The tubes were of three widely different textures obtained by the deformation techniques I, III and VI. In this case the final dimension of the tubes were the same, outer diameter 10.7 mm and wall thickness 0.7 mm. The tubes I, III and VI were subjected to tensile testing, closed-end burst testing, and open-end burst testing. The tensile tests were made on a conventional electronic-mechanical machine, at a strain rate of 0.02 per minute. For burst testing, the specimens were connected to a high-pressure oil supply capable of giving a steady rate of volume increase inside the specimens, corresponding to a strain rate of 0.02 per minute. The pressure was recorded with an electronic pressure gauge. During testing, the length and diameter of the specimens were continuously recorded. For the diameter measurement, a special extensometer was constructed based on three differential-transformer strain gauges separated by 120°, but in perpendicular contact with the outside of the tube specimen. The strain recordings had to be interrupted when necking or local bulging started. To follow the strain to fracture, a square photogrid was applied to the specimens. Measuring the squares before and after testing defined the effective strain and the strain ratio at each point of the specimen after failure. The uniform strain in the non-bulged part of the broken specimens was in acceptable agreement with the extensometer recordings.

Texture characterization. The textures of the tube specimens were determined by X-ray diffraction, using the

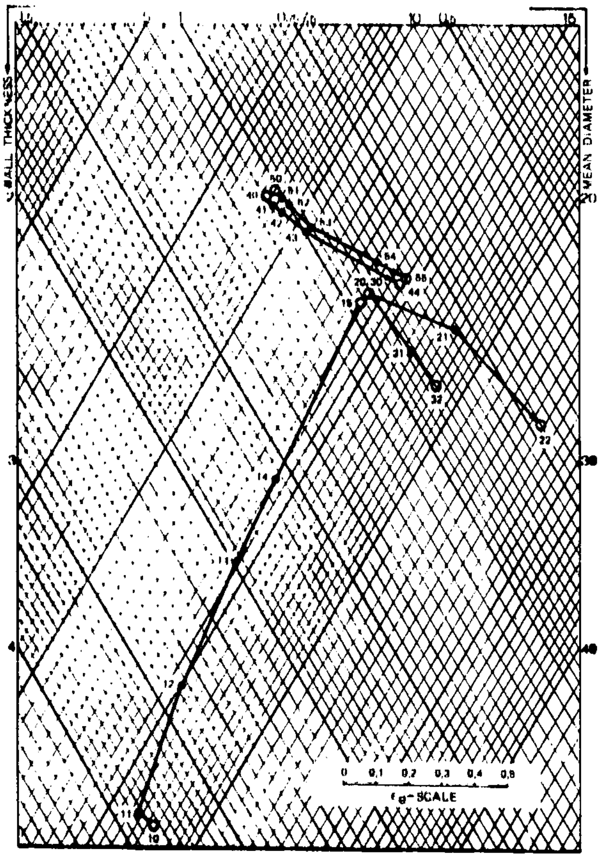

Figure 10. Double-logarithmic strain diagram with strain paths obtained with deformation techniques I, II and III.

inverse pole figure technique. X-ray diffraction specimens were prepared with chemically polished surfaces perpendicular to the radial, tangential, and axial directions, composite specimens being necessary for the latter two. The recordings were made with CoK_{α} radiation in a

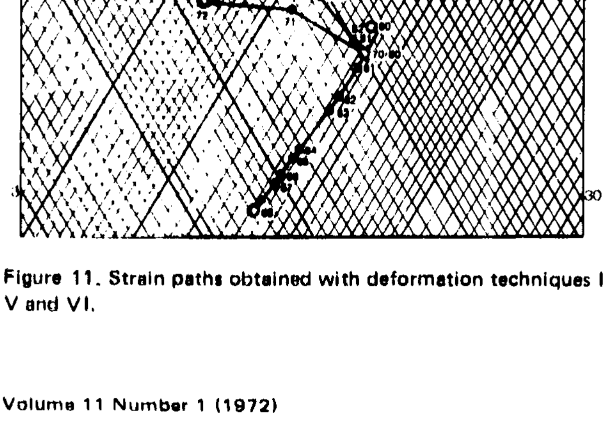

Figure 11. Strain paths obtained with deformation techniques IV, V and VI.

rotating specimens holder by scanning from 2θ 36° to 90° to cover reflections from ten crystallographic planes (see Table VIII). The texture coefficient T_q for the q^{th} reflection was calculated with the formula

$$T_q = 10 \cdot \frac{I_q/I_q^0}{\sum_{i=1}^{10} (I_i/I_i^0)} \qquad 12$$

where I_q and I_i are experimentally determined, integrated intensities evaluated as the area under the respective peak, and where I_q^0 and I_i^0 are intensities calculated for a texture-free specimen (see Table VIII (15)). The calculated intensities were in acceptable agreement with recordings from a randomized specimen of filings. The procedure and formula used are in accordance with Harris (16).

Texture coefficients of all 30 reflections from each triple specimen are normally presented in three 30° sectors of a stereographic projection. However, such a large amount of data would be difficult to survey here; instead the data are condensed into two representative parameters.

The texture of any polycrystalline material is completely described by a distribution function $w(\varphi, \omega, \psi)$, where the angles φ, ω, ψ define the orientation of a single grain (Figure 12). The function implies that $w(\varphi_1, \omega_1, \psi_1)$ $\sin\varphi_1\, d\varphi\, d\omega\, d\psi$ is the volume fraction of grains with crystal orientation within a small angular range ($d\varphi$, $d\omega$, $d\psi$) around the orientation ($\varphi_1, \omega_1, \varphi_1$). A function of this type may be expanded into a series of generalized spherical harmonics

$$w(\psi, \omega, \psi) = \sum_{l=0}^{\infty} \sum_{m=-l}^{l} \sum_{n=-l}^{l} W_{lmn} Z_{lmn} (\cos\psi) e^{-jm\omega} e^{-jn\psi} \qquad 13$$

Here W_{lmn} are the coefficients of the terms in the series, and Z_{lmn} $(\cos\varphi)$ are generalized Legendre functions. The significance and formalism for the use of spherical harmonics in describing texture have been developed by Roe (17), from whom some of the present notations are borrowed, and have recently been thoroughly developed by Bunge (18).

Reflexion symmetry of texture with respect to the three principal tube planes is, as previously stated, a consequence of the parallelism between principal strain directions and the principal tube directions. Also, inverse pole figures from the three principal directions only must be interpreted assuming such a reflexion symmetry. With the inherent symmetry of the hcp crystal, the number of W_{lmn} that are independent and non-zero are reduced to the *lmn* combinations, 000, 200, 220, 400, 420, 440, etc.

The coefficients W_{lmn} for the first few terms in the series are of interest because they describe the main feature of the texture, with W_{000} corresponding to the average distribution. Since the summation of all volume fractions must be 1, the W_{000} has a constant value for both textured

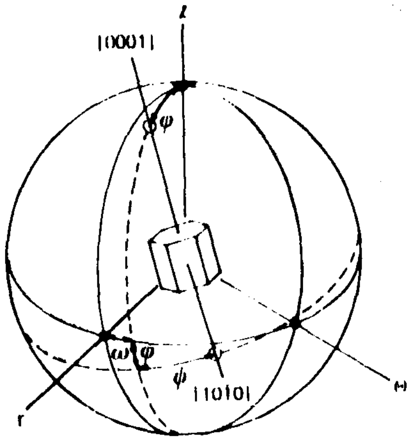

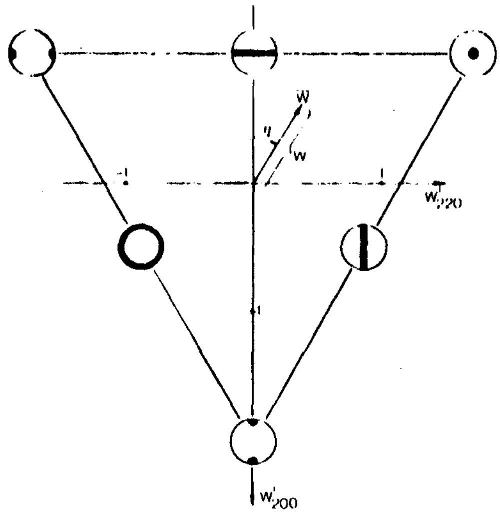

Figure 12. The orientation of a crystal in relation to the principal directions of a tube.

Figure 13. Graphical representation of textures in a Cartesian and a polar coordinate system. Equilateral triangle outlined by extreme textures.

and non-textured materials. The coefficients W_{200} and W_{220} express the main feature of the deviation from randomness or isotropy. The coefficients of higher order describe the deviation from isotropy in more detail. Evidence that only the basal pole orientation is included in the first order is that n is zero in W_{200} and W_{220}, i.e., the rotation around [0001] as expressed by the angle ψ is unimportant.

The coefficients W_{lmn} can be expressed explicitly as integrals of the distribution function w. After disregarding some normalizing constants and eliminating the angle ψ, the modified W'_{200} and W'_{220} are

$$W'_{200} = \int_0^\pi \int_0^\pi w(\psi,\omega)\,(3\cos^2\psi - 1)\sin\psi\, d\psi\, d\omega \qquad 14$$

$$W'_{220} = \sqrt{3}\int_0^\pi \int_0^\pi w(\psi,\omega)\sin^3\psi\cos 2\omega\, d\psi\, d\omega \qquad 15$$

These formulae can not be used for the experimental determination of W_{200} and W_{220} because $w(\varphi,\omega)$ is not known. However, the formulae are useful in illustrating the significance of W_{200} and W_{220}. Table V considers some special cases of basal pole distribution, from which $w(\varphi,\omega)$ may be estimated.

For graphical representation of textures a Cartesian coordinate system of W'_{200} and W'_{220} is chosen with the axes oriented as in Figure 13. Plotting the six extreme textures, these form an equilateral triangle (Figure 13). The three more moderate textures are plotted as schematic pole figures in relation to the equilateral triangle in Figure 14. They fall on the vertical line through the centre of the triangle. The centre is marked with a pole figure indicating random texture. For reasons of symmetry the triangle is completed with another six moderate fibre textures, which makes Figure 14 very similar to the texture rose. Like the texture rose, it not only contains information on the type of texture, but also on the sharpness of texture. The position of a plotted texture can be defined by a texture vector $\overline{W}$ (Figure 13). The angle of this vector is identified as the *texture ratio* η and the magnitude is called the *texture sharpness W.*

$$\eta = \arctan\left(-W'_{220}/W'_{200}\right) \qquad 16$$

$$W = \sqrt{W'^{\,2}_{200} + W'^{\,2}_{220}} \qquad 17$$

Table V. The coefficients W'_{200} and W'_{200} for some special basal pole distributions

Basal Pole Orientation		W'_{200}	W'_{220}
All basal poles exactly parallel to the	radial direction	-1	$\sqrt{3}$
	tangential direction	-1	$-\sqrt{3}$
	axial direction	2	0
All basal poles evenly distributed but exactly perpendicular to the	radial direction	1/2	$-\sqrt{3/2}$
	tangential direction	1/2	$\sqrt{3/2}$
	axial direction	-1	0
All basal poles evenly distributed within limits defined by the angle φ from the axial direction	$60° < \varphi < 120°$	-0.75	0
	$0 < \varphi < 60°$, $120° < \varphi < 180°$	0.75	0
	$0 < \varphi < 30°$, $150° < \varphi < 180°$	1.37	0

Disregarding some proportional constants but keeping the factor $\sqrt{3}$ in the foregoing expression for W'_{200} and W'_{220} gives an equilateral triangle, showing the equivalence of the three principal directions, when the maximum texture sharpness equals two ($W = 2$). This is because textures on the middle of the sides of the triangle have the basal pole distributed perpendicular to one direction. This implies that the distribution has lost one degree of freedom and hence the sharpness W should have the value one. Textures in the triangle corners have all basal poles parallel to one direction, meaning that two degrees of freedom are lost and the sharpness W should have the value two.

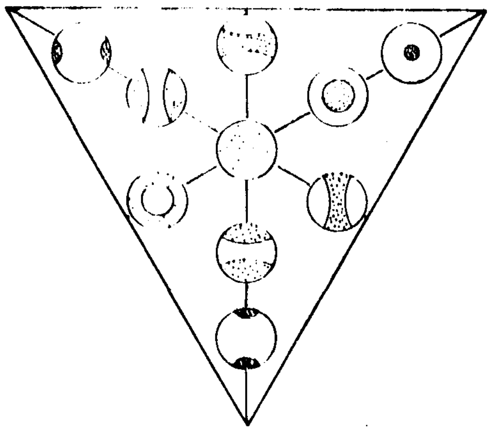

Figure 14. Positions of fibre textures in relation to the equilateral triangle.

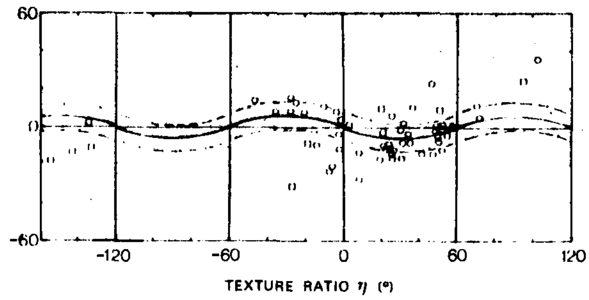

Figure 15. The relation between anisotropy ratio and texture ratio illustrated by $(\eta - \nu)$ as a function of η. The error limits $\pm 11^\circ$ are indicated by dashed curves.

The formalism for evaluation of W'_{200} and W'_{220} from the 30 texture coefficients determined for each triple specimen is presented in the appendix. The final result is two explicit expressions suitable for routine computing. Repeated texture determinations from a series of specimens taken from the same tube indicate that the total error from specimen preparation, X-ray diffraction and evaulation is ± 0.04 in W'_{200} and W'_{220}. When presented graphically in relation to the equilateral triangle, a texture is plotted as a circle with the radius 0.04, to indicate the range within which the true texture probably falls. The error in the texture sharpness is also ± 0.04, while the error in the texture ratio is smaller the greater the texture sharpness, as is shown by the graphical representation.

Mechanical anisotropy characterization. The Wheeler and Ireland technique for determination of the Knoop-hardness yield locus was used as a rapid method of defining the main features of mechanical anisotropy (19). Though the technique lacks a solid theoretical basis, it has given yield loci in good agreement with conventional techniques (20). The Knoop hardness is measured with six separate orientations of the indenter and the hardness values are plotted in a deviator stress diagram for six separate stress ratios. The yield locus may be fitted by hand to the six points, but here computer fitting of an ellipse was made standard procedure. The general equation of an ellipse contains only five constants, which motivated a least-squares method to utilize all six experimental points. The elliptical yield locus is characterized by the orientation β of the major axis, by the eccentricity and by the geometric mean of half the major and minor axes. Based on these parameters, the *anisotropy ratio* ν is defined as equal to $2(90 - \beta)$, the *anisotropy degree* A as equal to the eccentricity and the *mean hardness* H as equal to the geometric mean.

The Knoop measurements were made with 500 gram load on chemically polished surfaces. The maximum error in the eccentricity, i.e., the degree of anisotropy, is estimated to ± 0.04. The error in the anisotropy ratio $\Delta\nu$ is smaller the greater the degree of anisotropy, $\Delta\nu = \pm 10, 6, 3, 2^\circ$ for $A = 0.5, 0.6, 0.7, 0.8$, respectively.

Results and discussion

Texture and mechanical anisotropy. It was predicted from considerations of symmetry that the anisotropy ratio ν equals the texture ratio η. To check this prediction, $(\eta - \nu)$ is plotted as a function of η in Figure 15 for all specimens from the deformation experiments. Since the strain history should not affect this relation, results from a number of odd specimens from both tubular and strip material are included. Values less accurate due to low W and A are plotted as squares, while values with maximum error $\Delta\eta = \pm 5^\circ$ and $\Delta(\eta - \nu) = \pm 11^\circ$ are plotted as circles. A deviation from the prediction $(\eta - \nu) = 0$ outside the error limits is apparent. There are very good reasons that $\nu = \eta$ for $\eta = n \cdot 60^\circ$, i.e., for rotational symmetric textures. However, a periodic deviation seems reasonable, because of the two separate ways of defining and determining the η and ν. Least-squares fitting of a sine function yields

$$\nu = \eta + 6 \sin 3\eta \qquad 18$$

Most plotted values of $(\eta - \nu)$ are within the error limits from this relation. Those few values not within the error limits, plotted as circles in Figure 15, must be regarded as representing textures of a more complex type, e.g., originating from inhomogeneous deformation.

The degree of anisotropy A is smaller in strain-hardened material than in recrystallized. This might be interpreted that strain hardening counteracts slip deformation more than twinning. Among those specimens investigated both before and after recrystallization, seven had a texture sharpness change less than 0.1. Based on these seven specimens the following relation for the hardness sensitivity of the degree of anisotropy is derived:

$$\frac{1}{A} \cdot \frac{\partial A}{\partial H} = -(3.5 \pm 1.4) \cdot 10^{-3} \qquad 19$$

All values of A determined were corrected to A', as corresponding to the soft-annealed mean hardness 185 KHN. The corrected values of A' are plotted in Figure 16 as function of W. In an isotropic material $W = 0$ and $A' = 0$, while for a single crystal with $W = 2$, A' can be assumed to be approximately 0.9. One equation fulfilling these boundary conditions is $A' = 0.9(W/2)^a$. Using the experimental data, the exponent $a = 0.2$ has been determined by a least-squares method. The following equation describes the relation between corrected anisotropy ratio and texture sharpness:

$$A' = 0.9(W/2)^{0.2} \qquad 20$$

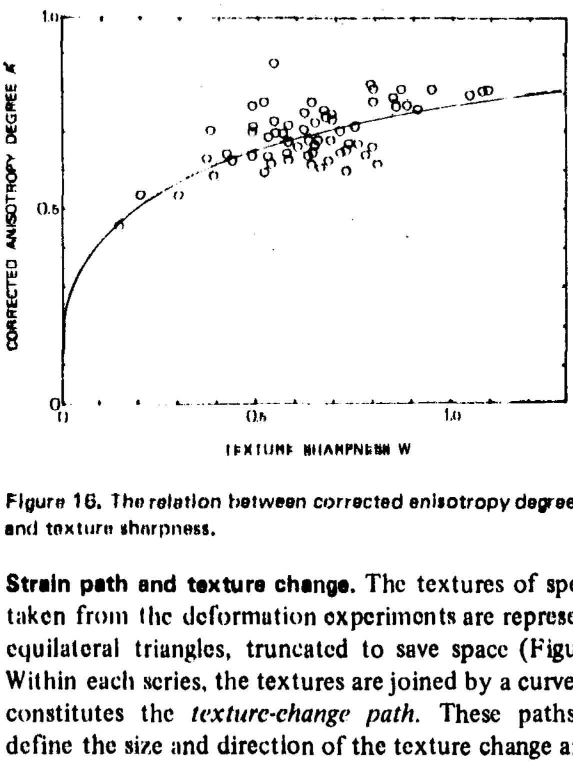

Figure 16. The relation between corrected anisotropy degree and texture sharpness.

Strain path and texture change. The textures of specimens taken from the deformation experiments are represented in equilateral triangles, truncated to save space (Figure 17). Within each series, the textures are joined by a curve, which constitutes the *texture-change path.* These paths which define the size and direction of the texture change are to be correlated with the corresponding strain paths in Figures 10 and 11.

For the series 30-32, 40-44, 50-55, 60-68 and 70-72 the texture-change path and the strain path are approximately parallel. For series 10-15 and 80-85, there is no such parallelism, but the texture-change path is parallel to the upper side of the triangle. The reason is that the starting textures of specimens 10 and 80 are already so close to the upper side that there is no room for texture change parallel to the strain path. This is because the sides of the equilateral triangle are defined as impossible to cross, and because it ought to be difficult to reach the sharper texture, by an approach towards the side. The texture change occurs instead in the direction of the projection of the strain on the triangle side. The series 40-44 and 50-55, which differ only in the heat treatment of the starting material, have parallel texture-change paths. A general rule for the

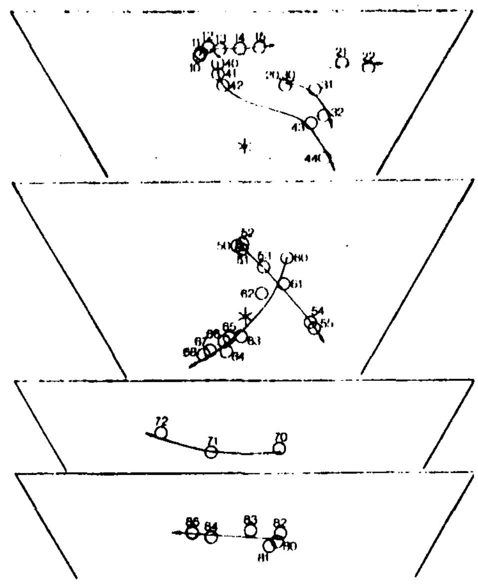

Figure 17. Texture-change paths obtained in deformation experiments.

texture-change path for any starting texture is suggested:

A texture-change path is parallel to its corresponding strain path, until one of the triangle sides is approached, where the texture-change path deviates to become parallel to the projection of the strain path on the triangle side.

A texture is stable if the texture ratio has not changed during the last stage of deformation. However, it is unchanged in very few cases and so, when judging the stability of a texture, consideration must be given to the degree of deformation, in some cases to the length of the projection of the strain path and to the texture sharpness. The latter must be considered because a certain texture change might alter the texture ratio much more at a low texture sharpness. Stable textures should have been reached by specimens 15, 65-68 and 85. Specimens from some other tubes, deformed by technique I with a strain ratio of 25°-27°, were also considered to have reached a stable texture. The relation between these stable texture ratios η and the strain ratio α is shown in Figure 18, where $(\eta - \alpha)$ is plotted as a function of α. For most textures $(\eta - \alpha) = 0$, and the only texture somewhat different is the one for specimen 15. Perhaps the texture of number 15 was not truly stable. Together with the very strong symmetry reasons that $(\eta - \alpha) = 0$ for $\alpha = n \cdot 60$, Figure 18 is the proof that η equals α for stable textures, verifying the texture rose in Figure 4 at least quantitatively.

Replacing η with α in Equation 18 gives the relation between stable anisotropy ratio and the strain ratio $\nu = \alpha + 6 \sin 3\alpha$. This is a verification of the predicted relationship shown in Figure 6. The sine function is only a minor modification, since the yield locus for $\alpha = 30°$ has its major axis angle $\beta = 72°$ instead of 75° as was predicted. All

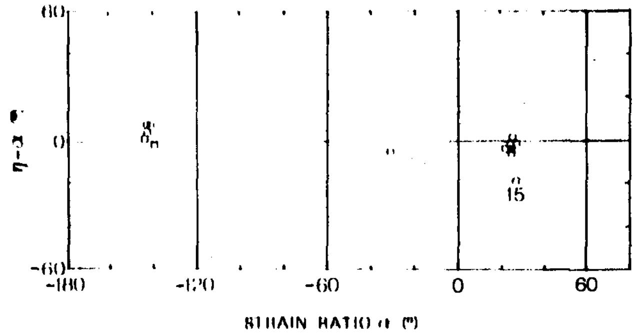

Figure 18. The relation between stable texture ratio and strain ratio illustrated by (η - α) as a function of α.

yield loci for $\alpha = 30° + n \cdot 60°$ should be modified accordingly, while the symmetric yield loci for $\alpha = n \cdot 60°$ are still true.

The rule for the texture-change path and the relation η - α make it possible to construct a number of texture-change paths from a starting texture O to stable textures S, under the effect of any strain ratio. In a texture-free starting material these paths go straight from the centre of the triangle towards the sides with η always equal to α. In a textured starting material some texture-change paths deviate as they approach the triangle sides (Figure 19). For some strain ratios the question arises as to whether the deviation occurs towards a stable texture or in the direction of the projection of the strain path. Specimen 20-21 indicates the latter (Figure 17), because the texture is changed towards the right corner of the triangle. However, proof cannot be extracted from the present data. The question is of great importance. If deviation occurs towards a stable texture, only the prevailing strain ratio influences the resulting texture. If the deviation occurs in the direction of the projection, the starting texture may also influence the resulting texture. This suggests that the

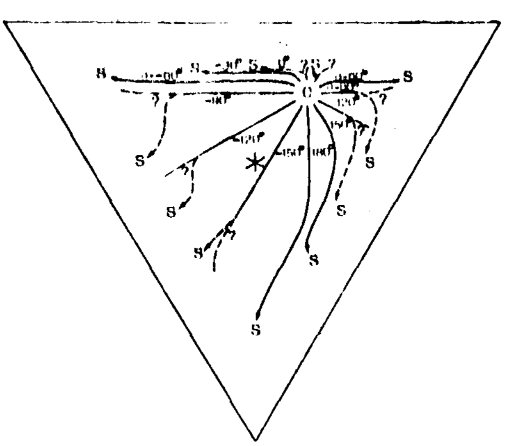

Figure 19. Constructed texture-change paths from starting texture O to stable textures S under the influence of separate strain ratios.

material might retain the memory of its previous strain history. An implication of this would be that the texture rose is not valid under all circumstances.

The parameter *texture-change rate* is introduced to express the texture change occurring per unit effective strain along the texture-change path, until the texture becomes stable with respect to sharpness. If the distance between two subsequent textures in the equilateral triangle is ΔW, i.e., $|\Delta W|$, and if the effective strain causing the change is $\Delta\epsilon_e$, the texture-change rate is defined by $\Delta W/\Delta\epsilon_e$. The heavy deformation of series 10-15 gave a small texture change compared to most other series, which means the texture-change rate varies. It seems probable that the projection of the strain path on the texture-change path is one of the factors governing the rate. All else being constant, $\Delta W/\Delta\epsilon_e$ should be proportional to $\cos(\alpha - \Delta\eta)$, where $\Delta\eta$ is the direction of the straight line between the two textures in their graphical representation. Calculated values of $\Delta W/(\Delta\epsilon_e \cos(\alpha - \Delta\eta))$ are given in Table VI for most of the deformation steps. The values range from 0.8 to 2.5, except for a high value for step 40-42, and low values for steps 14-15 and 84-85. No reason for the high value is evident, while the low values are for texture changes close to stability. No other systematic variation in $\Delta W/(\Delta\epsilon_e \cos(\alpha - \Delta\eta))$ is apparent and hence the conclusion is that this parameter has a constant value, except close to textures stable with respect to sharpness. Average and

Table VI. Evaluation of texture-change rate between specimens from deformation experiments

Step Between Specimen No.	Deformation $\alpha°$	Deformation $\Delta\epsilon_e$	Texture Change $\Delta\eta°$	Texture Change ΔW	$\frac{\Delta W}{\Delta\epsilon_e \cos(\alpha - \Delta\eta)}$
12-13	23	0.42	96	0.10	0.8
13-14	24	0.28	87	0.15	1.2
14-15	27	0.61	87	0.14	0.5
20-21	115	0.28	66	0.46	2.5
30-31	144	0.22	101	0.23	1.4
31-32	145	0.13	165	0.20	1.6
40-43	129	0.16	124	0.81	5.1
43-44	120	0.33	150	0.28	1.0
50-53	133	0.15	130	0.24	1.6
53-55	122	0.33	142	0.60	1.9
60-61	- 145	0.12	- 175	0.21	2.0
61-62	- 144	0.11	- 109	0.19	2.1
62-65	- 144	0.25	- 143	0.42	1.7
65-68	- 140	0.20	- 123	0.22	1.2
70-71	- 56	0.25	- 92	0.51	2.5
71-72	- 84	0.27	- 70	0.41	1.6
80-83	- 35	0.23	- 73	0.28	1.6
83-84	- 33	0.23	- 104	0.21	2.8
84-85	- 31	0.50	- 69	0.16	0.4

standard deviation of the values between 0.8 and 2.8 are 1.7 ± 0.6. Thus, the texture-change rate is given by

$$\Delta W/\Delta\epsilon_e = 1.7 \cos(\alpha - \Delta\eta) \qquad 21$$

This formula certainly has a low accuracy, since experimental errors have been accumulated, but it still is of importance in prescribing production routes to reach specific textures.

Yield locus and texture softening. The texture and mechanical anisotropy of the three mechanically tested tube materials I, III and VI are given in Table VII. The true stress-effective strain curves recorded are shown in Figure 20, marked with $\gamma = 0°$ for tensile testing, $\gamma = 90°$ for closed-end burst, and $\gamma = 120°$ for open-end burst testing. The strain paths to fracture are shown in Figure 21. The maximum effective strain must not be used in comparing the separate textures, because the tube material III in particular had variable dimensional tolerances, owing to the experimental state of the deformation technique. The strain paths have a tendency to bend towards $\alpha = 60°$, because the stress ratio in necking or bulging changes towards $\gamma = 60°$.

Table VII. Characterization of tube materials mechanically tested. Deformation hardening reduced by texture softening between 0.4 and 10 per cent strain

Tube	Texture		Mechanical Anisotropy		Mean hardness	Increase in σ_e Between ϵ_e 0.004 and 0.1 (kg/mm²)		
	$\eta°$	W	$\nu°$	A	(KHN)	$\gamma=0°$	$\gamma=90°$	$\gamma=120°$
I	28	0.54	48	0.80	169	21.2	14.7	10.6
III	76	0.48	82	0.63	177	12.9	19.2*	19.2
VI	−23	0.56	−34	0.63	180	18.2	12.1	11.8

*Extrapolated.

The mechanical tests offer an opportunity to check on the accuracy of the elliptical Knoop-hardness yield loci (Figure 22). The mechanical tests give three points on the

Table VIII. Planes indexed q or i in hcp zirconium, X-ray intensities I^0 of texture-free specimen, angles Φ_q between plane normal and basal pole, and $k_q = 3\cos^2\Phi_q - 1$.

Plane	Index q or i	I_q^0 or I_i^0	Φ_q	k_q
$10\bar{1}0$	1	0.91	90°	−1
0002	2	0.91	0	2
$10\bar{1}0$	3	3.51	61.47	−0.316
$10\bar{1}2$	4	0.53	42.60	0.626
$11\bar{2}0$	5	0.57	90	−1
$10\bar{1}3$	6	0.62	31.52	1.180
$20\bar{2}0$	7	0.09	90	−1
$11\bar{2}2$	8	0.67	57.88	−0.152
$20\bar{2}1$	9	0.47	74.79	−0.793
0004	10	0.09	0	2

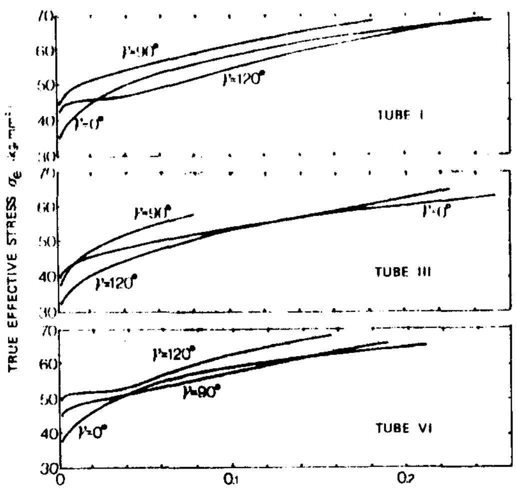

Figure 20. True stress-effective plastic strain curves for tensile, closed-end burst and open-end burst testing of tube material I, III and VI.

true yield locus. Best agreement was obtained using the stress at $\epsilon_e = 0.012$ and the conversion factor 3.9 KHN/(kg/mm²) (Figure 22). A yield locus at the strain $\epsilon_e = 0.012$ should not be considered true, because this strain is enough to cause a texture change as will be discussed.

Some of the stress-strain curves in Figure 20 display something like a yield-point phenomenon. This must be due to anisotropy, since it appears more or less pronounced, depending on the combination of tube material and testing method. Evidently the deformation causes a change in texture and anisotropy which alters the flow stress required. The stress increase between $\epsilon_e = 0.004$ and 0.1 varies from 10.6 to 21.2 kg/mm², because of strain hardening (Table VII). The greatest increase 21.2 kg/mm², is in tensile testing. Independent of the predicted regions for softening or hardening, tensile testing with $\gamma = 0°$ can

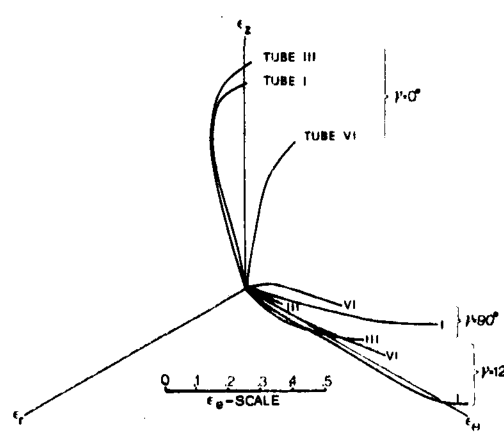

Figure 21. Strain paths followed during mechanical testing.

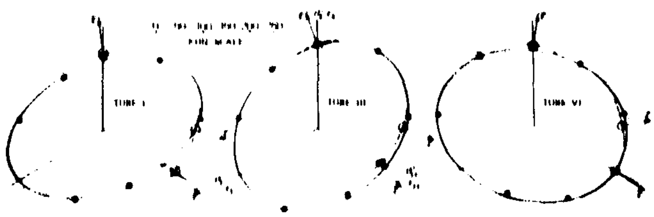

Figure 22. Elliptical Knoop-hardness yield loci together with parts of the true yield loci.

only result in texture softening, since the stable yield locus has its minor axis parallel to the stress vector. Thus pure strain hardening should increase σ_e somewhat more than 21.2 kg/mm². A reasonable assumption is 23 ± 2 kg/mm². Thus, the texture softening corresponds to the difference between 23 and the increases in σ_e given in Table VII.

The anisotropy ratios of the materials tested are plotted in Figure 9 as function of the stress ratios. A number for the texture softening is given inside each plotted point. All points fall within predicted regions of texture softening. The softening is, in general, greater the farther the plotted point is from the stable ν - γ relation. This is evidence for the predicted behaviour, even if not definite proof. Texture hardening apparently is not so common, since it requires unusual testing methods or extreme textures.

Texture softening occurs at the very beginning of the test, and is more or less completed before $\epsilon_e = 0.1$. With a texture-change rate as given by Equation 21, a strain of 0.1 should not change the properties appreciably. The free deformation under a given stress ratio in mechanical testing is different from the forced strain in the deformation experiments. An explanation for the observed behaviour might be that rapid texture change is obtained through abundant twinning, if the shear strain of the twins must not necessarily conform with a forced deformation.

Conclusions

1. Experiments on Zircaloy tubes have confirmed the predicted texture rose as describing the relation between the type of stable texture and mode of plastic deformation. In addition, the texture-change path has been developed and the texture-change rate evaluated as functions of plastic deformation.

2. An important but unanswered question is whether the starting texture might affect the final texture. Thus, under certain conditions the texture rose is perhaps not valid.

3. The predicted relation between type of texture and type of mechanical anisotropy, as manifested by the Knoop-hardness yield locus, have been examined and found to be valid with a minor modification. In addition, the degree of anisotropy has been found to correlate with the texture sharpness.

4. The predicted relation between type of mechanical anisotropy and the foregoing plastic deformation has been verified.

5. Mechanical testing of tubes of different textures has resulted in texture softening, in agreement with the predicted behaviour of zirconium alloy. Although not proof, this supports the predicted regions, of alternate softening and hardening.

Acknowledgments

The author is indebted to The Sandvik Steel Works and specially to Dr. J.O. Edström and the late G. Lagerberg for their substantial support during the accomplishment of the present work, which was also partly financially supported by the Swedish Board for Technical Development. I want to thank the late G. Lagerberg also for his personal interest and for the stimulating discussions with him. I am grateful to G. Ökvist for his contributions in developing the deformation techniques. I finally want to thank Prof. R. Kiessling, Director of Research and Development, for his kind permission to publish this paper.

APPENDIX

Evaluation of W'_{200} and W'_{220} from inverse-pole-figure texture data

The angle between the normal to the crystallographic plane q and the basal pole is denoted Φ_q and given in Table VIII for hcp zirconium with $c/a = 1.593$. Grains with the plane q normal oriented parallel to a principal direction p have possible basal pole orientations describing a circular line L_{pq} on the orientation sphere.

L_{zq} is defined by $\varphi = \Phi_q$ while $\omega = 0 \rightarrow \pi/2$, (Figure 23($a$)) L_{rq} is defined by $\varphi = \Phi_q$ while $\omega' = 0 \rightarrow \pi/2$, where from spherical trigonometry applied on the triangle ABC in Figure 23(b), $\cos\varphi = \sin\varphi' \sin\omega'$ and $\cos\omega = \cos\varphi'/\sin\varphi$.

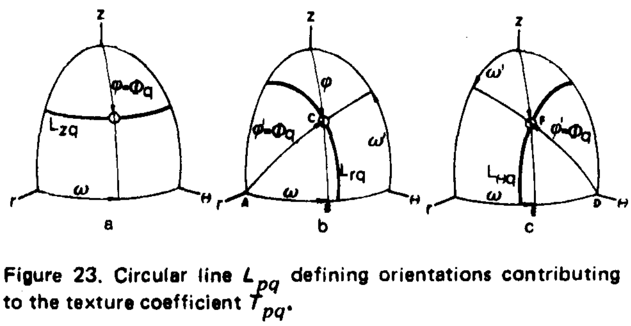

Figure 23. Circular line L_{pq} defining orientations contributing to the texture coefficient T_{pq}.

$L_{\theta q}$ is defined by $\varphi' = \Phi_q$ while $\omega' = 0 \rightarrow \pi/2$, where from spherical trigonometry applied on the triangle DEF in Figure 23(c), $\cos\varphi = \sin\varphi' \cos\omega'$ and $\sin\omega = \cos\varphi'/\sin\varphi$.

Integration of the function w along the line L_{pq} and dividing with the same integral of w_0 for texture-free material corresponds to the texture coefficient T_{pq} from inverse pole figure recordings of a surface perpendicular to the direction p.

$$T_{pq} = \int_{L_{pq}} w\,dL \Big/ \int_{L_{pq}} w_0\,dL \qquad 22$$

Series expansion yields

$$T_{pq} = 1 + \sum_{l=2}^{\infty} \sum_{m=1}^{l} \sum_{n=-l}^{l} W_{lmn} K^{pq}_{lmn} \qquad 23$$

Disregarding some proportional constants, the same for both K^{pq}_{200} and K^{pq}_{220}

$$K^{pq'}_{200} = \int_{L_{pq}} (3\cos^2\psi - 1)\,dL \Big/ \int_{L_{pq}} dL \qquad 24$$

$$K^{pq'}_{220} = \int_{L_{pq}} \sin^2\psi \cos 2\omega\,dL \Big/ \int_{L_{pq}} dL \qquad 25$$

By replacing the two variables φ and ω with the constant Φ_q and the variable ω' and by integrating for $dL = d\omega'$, the expressions are condensed to

$$K^{rq'}_{200} = -k_q/2 \qquad K^{\theta q'}_{200} = -k_q/2 \qquad K^{zq}_{200} = k_q \qquad 26$$

$$K^{rq'}_{200} = k_q/2 \qquad K^{\theta q'}_{220} = -k_q/2 \qquad K^{zq'}_{220} = 0 \qquad 27$$

where $k_q = 3\cos^2\Phi_q - 1$ is given in Table VIII. To obtain the desired W'_{200} and W'_{220}, a least-squares procedure is applied in which the following summation is minimized:

$$\sum_p \sum_q \left[I^0_q \left(T_{pq} - 1 - W_{200}K^{pq}_{200} - W_{220}K^{pq}_{220} \right)^2 \right] \qquad 28$$

Here I^0_q, the X-ray intensity for a texture-free specimen, is introduced as a weighting factor (Table VIII). The statistical error in an X-ray recording is proportional to $\sqrt{I^0_q}$ and hence I^0_q is entered in the summation to give the more accurate T_{pq} more weight. The final expressions for W'_{200} and W_{220} used routinely are

$$W'_{200} = \frac{1}{39} \sum_q \left[I^0_q k_q \left(2T_{zq} - T_{rq} - T_{\Theta q} \right) \right] \qquad 29$$

$$W'_{220} = \frac{\sqrt{3}}{39} \sum_q \left[I^0_q k_q \left(T_{rq} - T_{\Theta q} \right) \right] \qquad 30$$

The factors 1/39 and $\sqrt{3}/39$ are introduced to give $W'_{200} = -1$ and $W'_{220} = \sqrt{3}$ for a single crystal with a radial basal pole. The number 39 is an assumption based on the fact that the greatest texture coefficient recorded among hundreds of specimens was 12.6 for {11$\bar{2}$0}. Probably this specimen surface was almost 100 per cent {11$\bar{2}$0} and a single crystal can be expected to give the texture coefficient 13, which requires the factors 1/39 and $\sqrt{3}/39$. It should be emphasized that this estimation is dependent on the divergence of the X-ray beam, i.e., characteristic only for the specific diffraction set-up used. This uncertainty does not influence the texture ratio derived, but only the texture sharpness values by a constant factor.

References

(1) W.G. Burgers, J.D. Fast and F.M. Jacobs. *Z. Metallk.* 29: 410 (1937).
(2) R.K. McGeary and B. Lustman. *J. Metals.* 3: 994 (1951).
(3) I.L. Dillamore and W.T. Roberts. *Met. Rev.* 10: 302, 358 (1965).
(4) M.L. Picklesimer. *Electrochem. Technol.* 4: 289 (1966).
(5) P.L. Rittenhouse and M.L. Picklesimer. *Electrochem. Technol.* 4: 322 (1966).
(6) P.L. Rittenhouse. *J. Nuclear Materials.* 23: 183 (1967).
(7) P.L. Rittenhouse. *J. Nuclear Materials.* 24: 310 (1967).
(8) B.A. Cheadle and C.E. Ells. *Trans. AIME.* 233: 1044 (1965).
(9) K.P. Steward and B.A. Cheadle. *Trans. AIME.* 239: 504 (1967).
(10) B.A. Cheadle, C.E. Ells and W. Evans. *J. Nuclear Materials.* 23: 199 (1967).
(11) D.O. Hobson. *ASTM STP.* 458: 37 (1969).
(12) E. Tenckhoff and P.L. Rittenhouse. *ASTM STP.* 458: 50 (1969).
(13) R. Hill. *The Mathematical Theory of Plasticity.* Oxford Univ. Press, London, 1950.
(14) W. Johnson and P.B. Mellor. *Plasticity for Mechanical Engineers.* Van Nostrand, London, 1962.
(15) H.P. Klug and L.E. Alexander. *X-ray Diffraction Procedures.* Wiley, New York, 1954.
(16) G.B. Harris. *Phil. Mag.* 43: 113 (1952).
(17) R.-J. Roe. *J. Appl. Phys.* 36: 2024 (1965).
(18) H.J. Bunge. *Mathematische Methoden der Texturanalyse.* Akademie-Verlag, Berlin, 1969.
(19) R.G. Wheeler and D.R. Ireland. *Electrochem. Technol.* 4: 313 (1966).
(20) D. Lee, F.S. Jabara and W.A. Backofen. *Trans. AIME.* 239: 1476 (1967).

PRINCIPLES OF BURST TESTING OF ZIRCALOY CANNING TUBES AND FACTORS INFLUENCING THE RESULT

Krister Källstrom
Martin Svenzon

Summary

There are two principles of burst testing of tubes, open end burst testing and closed end burst testing. The difference between the two principles is described and the practical specimen set-ups are shown. The open end burst testing requires the lower internal pressure and yields the greater maximum circumferential expansion as evident from comparative testing of Zircaloy canning tubes.

Zircaloy tubes have a pronounced tendency for bending in burst testing. This is interpreted as plastic instability of a first kind as opposed to the second kind of instability initiating the growth of a bubble. The first kind of instability is explained as an effect of the anisotropy of textured Zircaloy tubes. In closed end burst testing, specimens kept straight by means of an internal telescopic rod, reach a maximum circumferential expansion 1.2 times greater than specimens free to bend.

The effect of a stiff pressure system is demonstrated in a comparative closed end burst testing, where a stiff pressure system gave maximum circumferential expansions 1.5 times greater than a pressure system that is soft or flexible due to the presence of compressed air. Another source of varying results is the tube itself. Thus, a wall thickness variation in Zircaloy canning tubes decreased the uniform circumferential expansion obtained in closed end burst testing.

1. Open end burst testing as compared to closed end burst testing

There are two basic principles of burst testing, open end burst testing and closed end burst testing. The principles and results of testing in two ways have previously been described by Steward and Cheadle(1). Here the comparison between open and closed end burst testing is repeated in order to emphasize the considerably different results obtained.

Stressing a thin walled tube with internal pressure according to the open end principle yields a uniaxial state of stress in the tangential direction, as illustrated in fig. 1. A tube with closed ends subjected to the internal pressure has a biaxial state of stress of 2:1 in the tangential and in the axial directions, respectively, fig. 1.

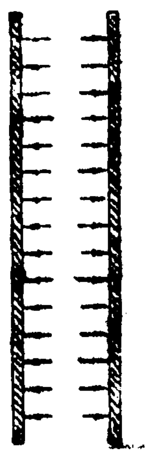

Open end burst testing

The internal pressure gives a tangential stress in the tube wall.

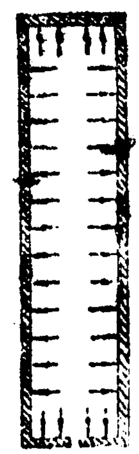

Closed end burst testing

The internal pressure gives a tangential stress and an axial stress with the ratio 2:1 in the tube wall.

Fig. 1 Principles of open end burst testing and closed end burst testing.

The practical arrangements of testing according to the two principles are shown in fig. 2. In open end burst testing a partly hollow rod is connected to a high pressure oil supply. O-rings of rubber are placed in grooves in both ends of the rod. The tube specimen is fitted on to the rod and provided with external support tubes at the two ends. When the volume of oil in the tube specimen is increased, the tube deforms by widening its diameter and shortening its length. The state of stress is truly unaxial if the frictional force from the O-rings is neglected. In closed end burst testing a telescopic rod is placed inside the tube specimen to keep it straight without restricting changes in length, for reasons further discussed below. The specimen is sealed off in the ends by standard tube couplings and connected to the high pressure oil supply, which is capable of giving a steady rate of volume increase inside the specimen The pressure is recorded on an x-y-recorder as a function of volume increase.

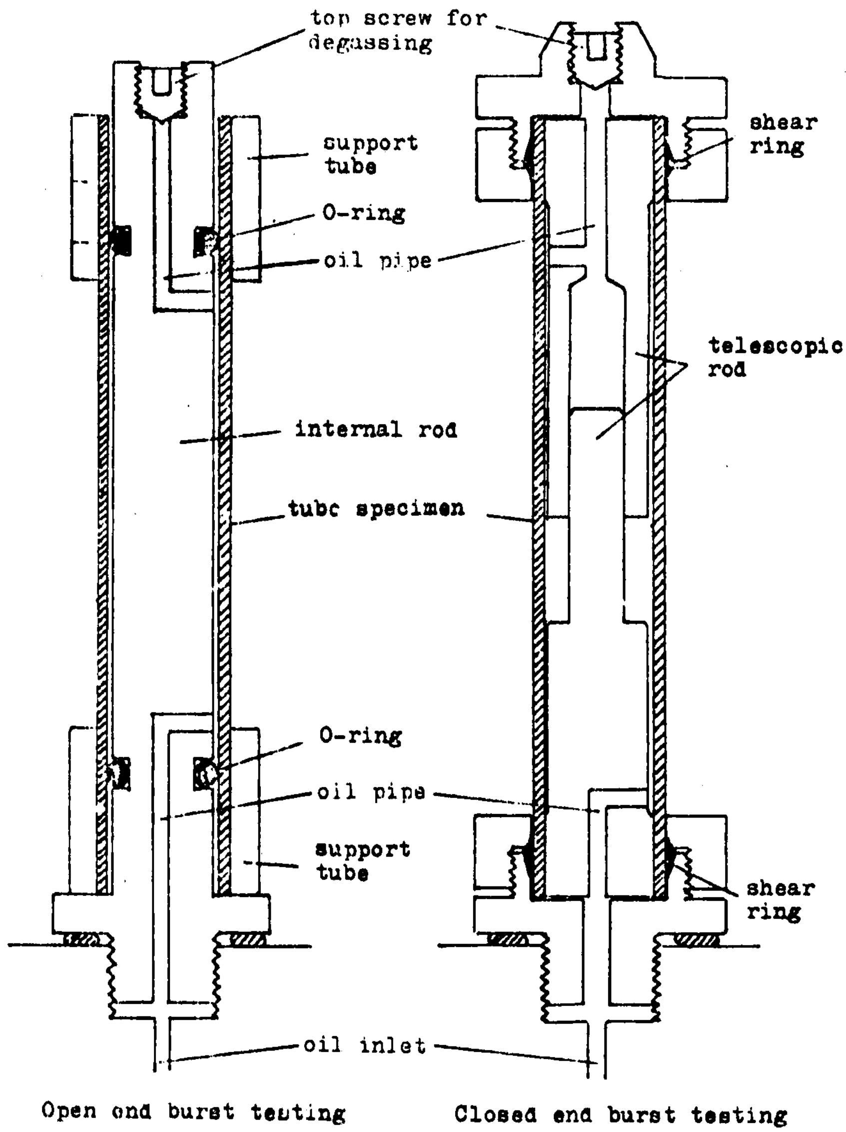

Fig. 2. Set-up for open end burst testing and for closed end burst testing. The tube specimen is 20 cm long and has a diameter of about 1 cm, which means the length scale is decreased and the width scale increased.

Zircaloy canning tubes were annealed to six levels of strength and ductility. Out of each level, five specimens were open end burst tested, five were closed end burst tested and two were tensile tested. After failure the specimens had the appearance shown in fig. 3 and 4. The mean values and standard deviations of the burst testing, and the individual values and standard deviations of the burst testing, and the individual values of the tensile testing are given in table 1.

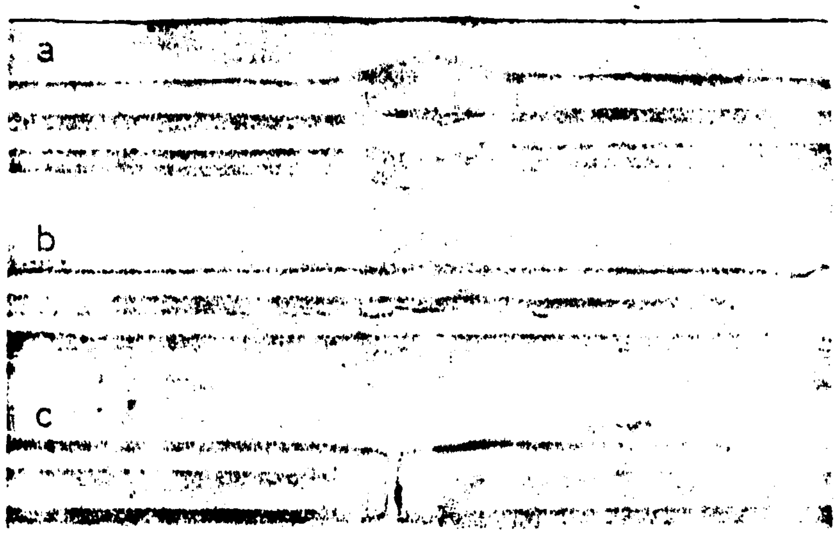

Foto no. 47892 Magnification 1.5

<u>Fig. 3</u> Hard Zircaloy tubing, material 1, after
a) open end burst testing, b) closed end burst testing, and
c) tensile testing.

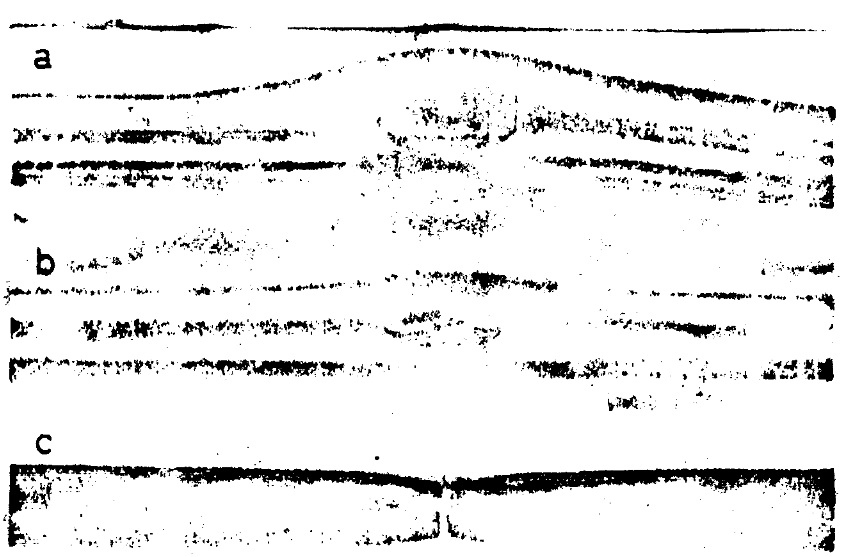

Foto no. 47893 Magnification 1.5

<u>Fig. 4</u> Soft Zircaloy tubing, material 5, after
a) open end burst testing, b) closed end burst testing, and
c) tensile testing.

The maximum tangential stress σ_θ was calculated from the maximum pressure p using the formula $\sigma_\theta = pd_i/2t$, where d_i is the original internal diameter and t the wall thickness. The circumferential expansion is calculated from the original circumference C_o and the circumference C after testing using the formula $100.(C-C_o)/C_o$. For the uniform expansion, C is measured on the cylindrical part of the specimen on one or both sides of the bubble, whereas for the maximum expansion, the largest C at the bubble is used.

The striking difference between open and closed end testing is the far greater maximum circumferential expansion obtained in open end burst testing. Even the hardest material which has only 3 percent maximum circumferential expansion in closed end burst testing, yields 50 percent in open end testing. The reason for this different behaviour is obvious. In open end burst testing the specimen shortens considerably, thus supplying material for the expansion. In closed end burst testing the specimen does not change so much mostly by wall thinning, and as a consequence, the failure occurs sooner.

Table 1. Results of open end burst, closed end burst, and tensile testing of Zircaloy canning tubes annealed to six levels of strength and ductility.

Level of strength and ductility		1	2	3	4	5	6
Open end burst testing							
Max. tangential stress		73±1	66±2	61±1	50±1	47±0	45±0
Circumferential expansion	uniform	4±2	4±1	6±1	13±3	12±2	13±4
	maximum	50±9	72±14	76±13	70±11	99±3	82±12
Closed end burst testing							
Max. tangential stress		85±1	80±2	71±5	61±1	60±2	59±2
Circumferential expansion	uniform	3±1	4±1	8±3	15±2	13±2	14±3
	maximum	3±1	7±3	17±9	32±10	36±14	45±13
Tensile testing							
Yield strength 0.2 %		58 61	55 55	50 50	40 39	36 37	34 34
Tensile strength		80 79	73 73	70 70	54 54	52 52	50 50
Elongation $\delta_{2''}$		16 18	20 20	20 20	32 32	32 24	26 32

Stress is given in kg/mm² and strain in percent.

2. Specimen free to bend as compared to specimen kept straight

Zircaloy canning tube specimens have a characteristic, strong tendency for bending, when plastically deformed under internal pressure. The tendency is apparent in open end burst testing, but in this case the specimen is always kept straight by the internal rod. In closed end burst testing the specimen was free to bend, before the use of a telescopic rod was made standard procedure. Bending certainly did occur, as illustrated by fig. 5.

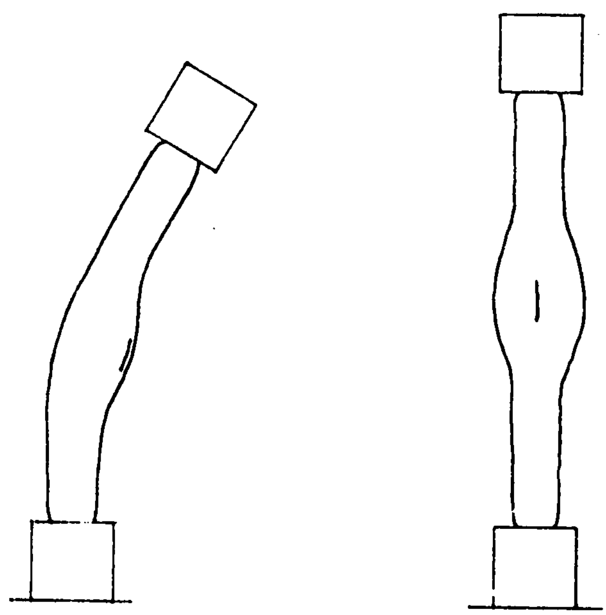

Tube specimen free to bend

Tube specimen kept straight with internal telescopic rod

Fig. 5. Behaviour of Zircaloy canning tube deformed in closed end burst testing.

The bending appeared very soon after the start of plastic deformation and increased gradually as the tube expanded. At a later stage in the testing the local bubble started to grow leading to the first failure, which always occurred on the concave side of the bent specimen. The bending is caused by a first kind of plastic instability as opposed to the second kind of instability initiating the growth of the bubble. The first instability could be explained as follows (2).

A tube of an isotropic material deformed in closed end burst testing does not change its length, because the shortening tendency of supplying material for the expansion is counterbalanced by the axial tensile stress component. Zircaloy tubes, however, are anisotropic due to a texture with dominantly radial basal poles as a normal feature, fig. 6. Radial basal poles make the radial direction hard and wall thinning unfavourable. Instead, Zircaloy tubes shorten during closed end burst testing in order to supply material for the expansion . In this process the specimen might very well deviate slightly from straightness.

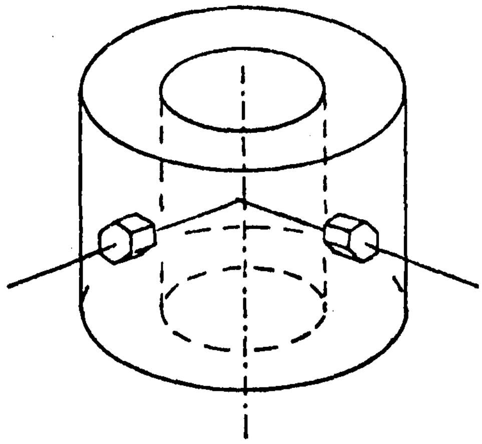

Fig. 6. Dominant orientation of zirconium crystals in Zircaloy canning tubes of standard production.

The state of stress in such a slightly bent tube subjected to internal pressure is varying, in that the axial stress component is smaller on the concave side. This can be realized from the action of the internal pressure as shown in fig. 7. Already a small deviation from straightness implies reduced axial tensile stress on the concave side, and accelerated shortening in the same side resulting in further bending.

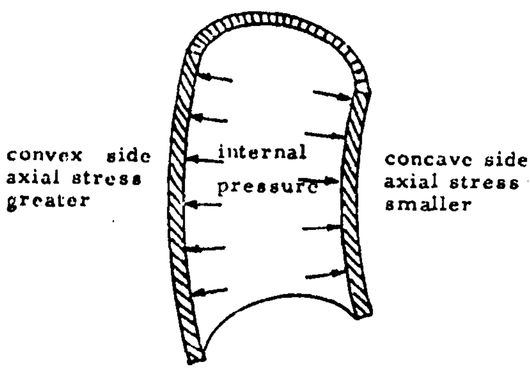

Fig. 7. Variation of the axial stress component in a bent tube during closed end burst testing.

The situation is typically unstable, which explains that this first kind of instability occurs early in the deformation process. As the deformation mostly takes place on the concave side, the wall thinning, although retarded, as well as the final fracture occur on this side.

In order to investigate the effect of bending, Zircaloy canning tubes were annealed to a medium level of strength and ductility, cut into specimens, and closed end burst tested. Nine specimens were free to bend and nine specimens were kept straight with the internal telescopic rod. Mean values and standard deviations of maximum tangential stress, and uniform and maximum circumferential expansion are compared in table 2. It is evident that the specimens kept straight reach a maximum circumferential expansion 1.2 times greater than specimens free to bend.

The reason for the greater expansion is considered to be that bending gives inhomogeneous deformation which inherently means low ductility. In a kept-straight tube, homogeneous deformation will occur until the final bubble starts growing, and even this latter deformation is more homogeneous because the bubble grows symmetrically around the tube.

Table 2. Results of closed end burst testing with specimen free to bend and with specimen kept straight by a telescopic rod. The specimens are of a medium level of strength and ductility.

Specimen		free to bend	kept straight
Max. tangential stress		72±1	73±1
Circumferential expansion	uniform	4±1	5±1
	maximum	10±3	12±5
Stress is given in kg/mm² and strain in percent			

Thus, the strain hardening capacity of the material all around the circumference contributes to the greater ductility displayed by the straight specimen.

3. The effect of a stiff pressure system

The results presented so far were obtained with a high pressure oil system with a stiffness of 500 kg/cm^5. Testing was also made with another pressure system charged with compressed air, which implies a stiffness orders of magnitude smaller.

Four Zircaloy canning tubes were annealed to a series of levels of ductility and 14 specimens were cut out of each tube. Half the number of specimens were tested with the soft pressure system under free-to-bend conditions (Method A), and the other half were tested with the stiff pressure system while kept straight (Method B).

The maximum circumferential expansions obtained are listed in table 3 as mean values and standard deviations 2). The values reached with specimens kept straight while tested with the stiff system, are 1.8 times greater for all levels of ductility. Roughly speaking the factor 1.8 could be regarded as built up by a factor of 1.2 from keeping the specimen straight and a factor of 1.5 attributable to the stiffness of the pressure system.

Table 3. Maximum circumferential expansion in closed end burst testing, in percent. Method A is carried out with specimens free to bend and with soft pressure system, method B with specimens kept straight and with stiffness pressure system.

Level of ductility	1	2	3	4
Method A	7±4	19±3	20±4	30±4
Method B	12±6	32±2	34±5	53±3

The stiffness effect can be explained in terms of the deformation rate. When the pressure tends to drop in the last stage of testing with a soft system, the air is expanding and the rate of volume increase in the specimen goes up drastically. This higher deformation rate requires higher deformation stress and reasonably gives lower ductility.

4. The effect of wall thickness variation

Closed end burst testing with a telescopic rod but with argon gas as pressure medium was made at 400°C. The specimens were taken from tubes of medium strength and ductility and were specially selected to represent a series of wall thickness variations ranging from 0.7 to 6.4 percent excentricity defined as $100\ (t_{max} - t_{min})/(t_{max} + t_{min})$. Here t_{max} is the maximum wall thickness and t_{min} the minimum. The uniform circumferential expansion was found to be smaller in tubes with high excentricity, as shown in fig. 8. The maximum expansion, on the other hand, did not correlate with the excentricity in this limited testing program.

The effect of excentricity found could be explained in the following way. If the wall is thinner on one side of the tube, deformation will take place on this side first. As the material is strain hardening, the deformation will spread all around the tube, but all the time the deformation and the strain hardening will have proceeded somewhat further on the thinner side.

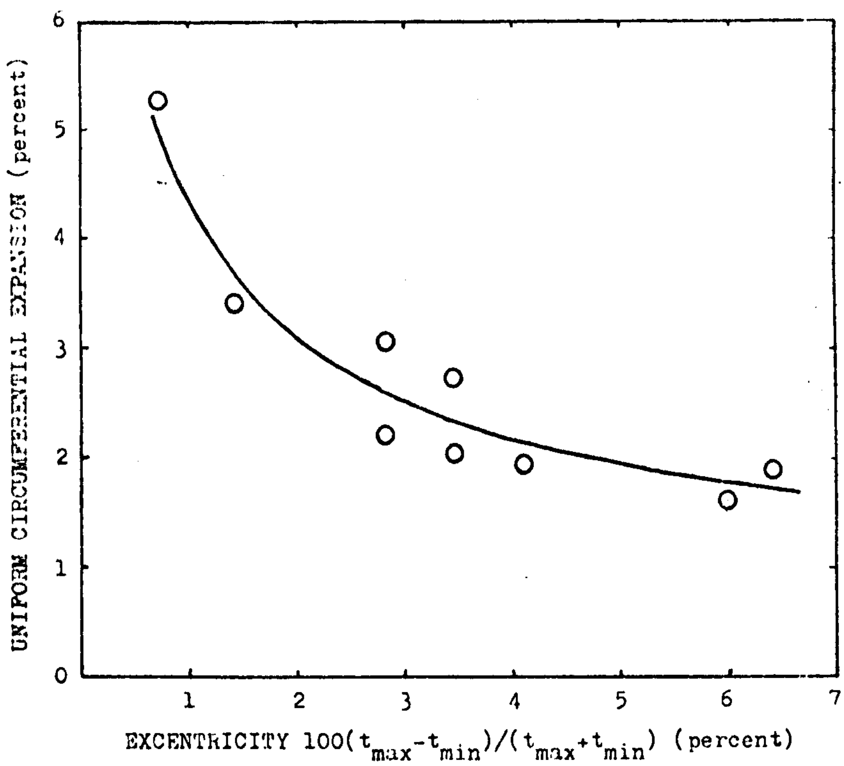

Fig. 8. Uniform circumferential expansion in closed end burst testing as a function of excentricity of Zircaloy canning tubes with wall thickness variation.

The rate of strain hardening is gradually decreasing during testing and at a certain stage it can no longer counterbalance the wall thinning taking place simultaneously This situation means plastic instability, initiation of local growth of a bubble, and ceasing uniform deformation, and the greater the excentricity the sooner it occurs.

References

1. K.P. Steward, B.A. Cheadle, Trans. AIME 239 (1967) 504.

2. O.K. Källström, J. Nucl. Mat. 31 (1969) 111.

DYNAMIC STRAIN AGING IN ZIRCALOY AND ITS DEPENDENCE OF COLD WORK, RECRYSTALLIZATION AND GRAIN SIZE

Krister Källström. Martin Svenzon
The Sandvik Steel Works, Sandviken, Sweden.

Presented at the symposium "Interstitials in Steel" in Uddeholm, April 12-14, 1972. Accepted for publication in Scandinavian Journal of Metallurgy.

Summary

The strain rate sensitivity (SRS) in Zircaloy-2 has been investigated by means of strain rate changes during hot tensile testing in the range 200-600°C. There was a pronounced minimum SRS at around 400°C, accompanied by plateaus in the strength vs. temperature relationships, by a ductility minimum, and by a strain hardening maximum. These are effects of dynamic strain aging originating from dissolved elements interacting with dislocations. The SRS minimum is associated with rapid generation of new dislocations at sources operating at a stress level more or less independent of the strain rate. The prime purpose of the work was to control the mechanical properties, and specially the 300-400°C creep strength, by the optimization of production parameters to derive maximum benefit from strain aging. It was found that cold work lowered the temperature of minimum SRS. This was reversed gradually as the degree of recrystallization was increased by annealing. Also, coarser recrystallized grain size gave a higher temperature of minimum SRS. A factor of 10 lower strain rate lowered the temperature of minimum SRS 20°C.

Extrapolation to creep rates indicates maximum effect at 280-350°C.

Introduction

Strain aging occurs in zirconium base alloys and specially in Zircaloy in the temperature range 200-500°C. The phenomenon manifests itself in tensile testing through the formation of yield point after interrupted loading [1], and through ductility and strain rate sensitivity minima [2, 3]. In creep testing considerably lower creep rates are recorded within the same temperature range, together with an abrupt increase in the apparent activation energy [4, 5].

A variety of mechanisms have been proposed to account for the strain aging. The formation of tin-rich precipitates [6], segregation of hydrogen [7], Cottrell locking of dislocations by impurity atmospheres [4], and other types of dislocation-interstitial interaction such as with oxygen are suggested [1]. Internal friction studies indicate that interstitial-substitutional complexes, for example oxygen-iron, create stress dipoles, which interact effectively with dislocations [8].

The strain aging effect on the mechanical properties of Zircaloy is of direct interest for the use of the alloy as canning tubes for fuel elements in nuclear reactors, implying a service temperature for Zircaloy in the range 300-400°C. Of prime concern are the creep strength and the ductility. Both these properties are closely related to the strain rate sensitivity (SRS). Thus, a low SRS, if applied in an extrapolation to creep strain rates, means that the creep strength is not so much less than the hot tensile strength. A high SRS, on the other hand, restricts a plastic instability from developing into necking and failure, as localized deformation gives higher strain rate, thereby strengening the potential necking. Since the dislocations play a critical role in strain aging, the Zircaloy structure, as controlled by the degree of cold work, recovery and recrystallization and by the grain size, should have a major influence on the strain aging-related properties. Thus, it was of direct interest to investigate the possible benefits from strain aging, specially as regards the 300-400°C creep strength, by optimization of production parameters. Hot tensile testing, with strain rate changes to reveal the SRS, was considered the most efficient experimental technique.

Of a more general interest is that zirconium as well as titanium, have solubility limits for interstitial oxygen as high as 6 and 14 wt.-%, respectively [9], i.e. magnitudes higher than the interstitial solubility in bcc-metals such as iron. This fact has been the basis for the use of hcp-metals in verifying models for solid solution strengthening mechanisms [10]. In the same way, strain aging effects in Zircaloy containing 0.10-0.14 wt.-% oxygen are probably magnified and may serve as an illustration of this type of phenomena in commonly used metals.

Experimental Procedure

Zircaloy-2 strip of the composition given in table I was cold rolled to a series of thicknesses, soft annealed and subsequently cold rolled 10, 20, 40, 60, and 75 % to the common final thickness 0.75 mm. The recrystallization behaviour was investigated through annealing to temperatures between 400 and 700°C for 4 hours, followed by tensile testing at room temperature. As normal for cold-worked metals, the relationships between yield strength and annealing temperature revealed three temperature ranges, a) a recovery range where the temperature dependence was low, b) a recrystallization range where the yield stress decreased rapidly with increasing temperature, and c) a grain growth range where the temperature dependence again was low. For each cold-rolling reduction, temperatures expected to give 0, 30, 60 and 100 % recrystallization were selected for annealing of the remaining main portion of the strip material. After the final anneal the result was checked against the yield strength-annealing temperature relationship, whereby obtained recrystallization degrees were found to be somewhat beside those aimed-for. This is presented in table II together with the grain sizes reached after full recrystallization.

The texture was analyzed by the inverse pole figure technique and found to be normal for rolled strip. The basal poles were perpendicular to the rolling direction and distributed between the transverse and the normal directions. The basal pole texture was nearly the same for all reductions and recrystallizations. Tensile specimens were machined for transversal loading.

Hot tensile testing was made in air between 200 and 600°C in an Instron tensile testing machine equipped with a furnace. The specimens were 150 x 15 x 0.75 mm with 100 mm as the effective test length. The strain rates used were a "normal" $8.3 \cdot 10^{-4}$ and "low" $8.3 \cdot 10^{-6}$ sec^{-1}, based on the original 100 mm test length. During normal strain rate testing the strain rate was repeatedly decreased by a factor of 10 for a few percent strain and then increased back to the normal rate again. During low strain rate testing the strain rate was repeatedly increased by a factor of 10 for a few percent strain and then decreased back to the low rate again.

Experimental results

Normal strain rate testing of standard material

Zircaloy strip cold-rolled 60% and recrystallized 100% was selected as a "standard" material for a more detailed description of the observed behaviour. The 0.2%-yield and ultimate tensile strengths, the uniform and total elongations, and the strain hardening exponent are presented as a function of testing temperature in figure 1. Total elongation means the elongation over originally 35 mm around the final failure. The strain hardening exponent is n in the well known formula $\sigma = K\epsilon^n$ [11]. It is evident how a plateau or a slight maximum appears in the yield strength curve in the same temperature range as a pronounced minimum total elongation and a maximum strain hardening exponent.

Strain rate reductions by a factor of 10 produced steps in the tensile curve, demonstrating the SRS, figure 2. Sometimes there was a transient behaviour in both ends of the step, similar to an inverse and a direct upper yield point. The stationary flow stress change $\Delta\sigma$ and the transient flow stress change $\Delta\sigma_t$ were recorded as shown in figure 2 and converted to true stress changes. The stationary SRS, denoted m, and the transient SRS, m_t, were calculated by the formulae:

$$m = \Delta\sigma/\sigma\Delta\ln\dot{\epsilon} \qquad (1)$$

$$m_t = \Delta\sigma_t/\sigma\Delta\ln\dot{\epsilon} \qquad (2)$$

Here σ is the average true flow stress level at the step in the tensile curve and $\dot{\epsilon}$ the strain rate. The SRS quantity m is the exponent in the formula $\sigma = K\dot{\epsilon}^m$ [11].

The SRS was dependent on the strain during a single test, since the stationary flow stress steps grew either larger or smaller and the transient flow stress steps grew smaller. This strain dependence of SRS was evaluated as $\Delta m/\Delta\epsilon$ and $\Delta m_t/\Delta\epsilon$ as a function of testing temperature. Based on this, all experimental SRS data was recalculated to be valid for zero strain and for a strain equal to the uniform elongation. The structure at uniform elongation was chosen as most representative of the material during secondary creep. The result is shown in figure 3, for both stationary and transient SRS. It is evident that the stationary SRS has a minimum and the transient SRS a maximum at around 400°C.

<u>Normal and low strain rate testing of all material</u>

The testing and evaluation procedure was repeated for all reduction-recrystallization combinations, both with normal and low strain rate. The interest was focused on the minimum of the stationary SRS at the strain of uniform elongation, since this is considered most relevant for high creep strength. The minimum value of the stationary SRS turned out to be constant $m = 0.005 \pm 0.005$ for normal strain rate and $m = 0.01 \pm 0.01$ for low strain rate for all material.

The temperature of minimum SRS on the other hand varied with the type of material. Higher cold-rolling reduction at zero recrystallization gave lower temperature of minimum SRS, figure 4a. Recrystallization reversed this effect, increasing the temperature again, figure 4b. Larger grain size of fully recrystallized material gave higher temperature of minimum SRS, figure 5a. The strain rate effect on the temperature of minimum SRS is shown in figure 5b. A factor of 10 lower strain rate yield 20°C lower temperature of minimum SRS, and extrapolation to creep strain rates of the order of 10^{-8} sec^{-1} implies approximately 60°C lower temperature for maximum benefit from low SRS in increasing the creep strength.

Discussion

Dynamic strain aging is manifested in tensile testing by plateaus or peaks in flow stress versus testing temperature curves, and by an increased strain hardening [12]. Also, low ductility accompanies dynamic strain aging, in steel referred to as blue brittleness [12]. All these phenomena are present in Zircaloy in the temperature range 400-500°C, figure 1. In view of this and previous reports on strain aging in zirconium-base alloys [1-5], it is concluded that true dynamic strain aging has been observed and investigated here. Without presenting any evidence for the actual solute-dislocation interaction mechanism, the formation of atmospheres of oxygen-substitutional complexes around dislocations is assumed. However, regardless of the exact interaction the following discussion should be valid.

According to Bergström et al [13], there is a lower temperature range where the solute mobility is sufficient for interaction with immobile dislocations. This makes the re-mobilization process improbable. In a higher temperature range the solute mobility is high enough for interaction with mobile dislocations. This increases the rate of immobilization. The temperature ranges overlap and at an intermediate temperature the total interaction or pinning effect is maximum. Deformation at this temperature is accommodated by a mobile dislocation density, which has to be maintained through abundant generation of new dislocations. To keep the dislocation sources activated a certain flow stress level is required more or less independently of the strain rate. This is the same as low SRS and explains the observed minimum stationary SRS in the temperature range of strain aging, figure 3.

Since the flow stress and the dislocation velocity are directly related, a strain rate change in the strain aging range also implies little variation in velocity. Instead the strain rate change is associated with a variation in mobile dislocation density. A support for this is the observed transient behaviour, figure 2, indicating that the mobile dislocation density requires some time for adjustment. Transients of this type are always doubtful, as they may originate wholly or partly from relaxations within the testing machine [14]. However, since the transients appeared only within the strain aging range, figure 3, they are considered as reflecting the variation in mobile dislocation density qualitatively.

The negative SRS for zero strain, figure 3, is not only due to the extrapolation, but was actually recorded at low strain in recrystallized material. A possible interpretation of negative SRS is based on the shortage of dislocation generation sources in a more perfect crystal. When the strain rate is decreased, there is a drop in flow stress followed by a transient increase up to a stress level higher than before the change. During the temporary flow stress drop some sources are permanently inactivated by solutes, and even after regaining stationary conditions fewer active sources are available. Thus, somewhat too few new dislocations are generated, requiring a higher stress to accommodate the strain rate. As the strain is increased to uniform elongation, the dislocation structure itself provides abundant generation sources readily activated, and there is no negative SRS.

Codl work increases and recrystallization decreases the immobile dislocation density, and smaller grain size gives a faster build-up of the immobile dislocation density. Thus, the effect of cold work, recrystallization and grain size on the temperature of minimum SRS, figure 4 and 5a, has to be explained on the basis of immobile dislocation density. At a given probability for re-mobilization, a higher immobile dislocation density implies a higher re-mobilization rate, assuming that the rate is equal to the product of the probability and density [13]. This lowers the upper limit of the temperature range for effective solute interaction with immobile dislocations, and as a consequence the temperature for maximum total interaction is lowered.

At lower strain rate immobile dislocations remain immobile for longer periods and also the average mobile dislocation velocity is lower. Thus, solute interaction with immobile as well as mobile dislocations requires a lower solute mobility. This explains the lower temperature of minimum SRS observed for lower strain rate, figure 5b.

Conclusions

1. Dynamic strain aging has been found to occur in the range 400-500°C during hot tensile testing of Zircaloy. The strain aging is accompanied by a minimum strain rate sensitivity (SRS).

2. The strain aging is considered as caused by dissolved elements interacting with both immobile and mobile dislocations. The interaction makes rapid generation of new dislocations necessary. The dislocation sources operate at a stress level more or less independent of strain rate, which means minimum SRS.

3. Cold work decreases and recrystallization and coarser grains increase the temperature of minimum SRS. The temperature range for interaction with immobile dislocations is lower for higher dislocation density and vice versa, and this influences the temperature for maximum total interaction, i.e. for minimum SRS.

4. A factor of 10 lower strain rate reduces the temperature of minimum SRS 20°C. Extrapolation to creep strain rates, indicates maximum benefit from strain aging on the creep strength at 280-350°C.

Acknowledgement

The authors are indebted to The Sandvik Steel Works for the possibility to accomplish the present work, and to the Swedish Board for Technical Development for financial support. We want to thank Professor R. Kiessling, Vice President, Steel Research and Development, for the permission to publish this paper.

References

1. VEEVERS, K., ROTSEY, W.B. & SNOWDEN, K.U., The effect of neutron irradiation and cold work on the strain-aging behavior of Zircaloy-2. In Application related phenomenon in zirconium and its alloys.
ASTM Special Technical Publication 458, pp. 194-209, ASTM, Philadelphia, 1969.

2. RAMACHANDRAN, V. & REED-HILL, R.E., Dynamic strain aging and ductility minima in zirconium.
Metallurgical Transactions 1(1970)2105-2109.

3. LEE, D., The strain rate dependent plastic flow behavior of zirconium and its alloys.
Metallurgical Transactions 1(1970)1607-1616.

4. FIDLERIS, V., The effect of texture and strain aging on creep of Zircaloy-2. In Application related phenomenon in zirconium and its alloys.
ASTM Special Technical Publication 458, pp. 1-17, ASTM, Philadelphia, 1969.

5. HOLMES, J.J., The activation energies for creep of Zircaloy-2.
Journal of Nuclear Materials 13(1964)137-141.

6. BANGERT, L., Fliessgrenzenerscheinungen in Zirkonium-Zinn-Legierungen.
Zeitschrift für Metallkunde 50(1959)265-274.

7. ÖSTBERG, G., Some observations on the ductility of zirconium alloys, with special reference to the effect of hydrogen.
Journal of the Institute of Metals 93(1965)223-228.

8. MISHRA, S. & ASUNDI, M.K., Internal friction due to oxygen-substitutional impurity atom complexes in zirconium.
Transactions of the Indian Institute of Metals 23(1970)73-79.

9. HANSEN, M., Constitution of binary alloys, pp. 1068, 1078.
McGraw-Hill, New York, 1958.

10. TYSON, W.R., Strengthening of hcp Zr, Ti and Hf by interstitial solutes - a review.
Canadian Metallurgical Quarterly 5(1967)301-332.

11. DIETER, G.E., Mechanical Metallurgy, pp. 237-256. McGraw-Hill, New York, 1961.

12. BAIRD, J.D., The effect of strain-ageing due to interstitial solutes on the mechanical properties of metals. Metallurgical Reviews No. 149(1971)1-18.

13. BERGSTRÖM, Y. & ROBERTS, W., The application of a dislocation model to dynamical strain ageing in α-iron containing interstitial atoms.
Acta Metallurgica 19(1971)815-823.

14. HALL, E.O., Yield point phenomena in metals and alloys, pp. 61-62. Plenum Press, New York, 1970.

Docent Krister Källström
Civilingenjör Martin Svenzon
Sandvikens Jernverks AB
Fack
811 01 Sandviken 1

Figure captions

Figure 1. Strength, ductility and strain hardening in Zircaloy strip cold-rolled 60 % and fully recrystallized as a function of tensile testing temperature.

Figure 2. Engineering stress-strain curve with steps produced by strain rate reductions. Measurement of stationary and transient flow stress change.

Figure 3. Stationary and transient strain rate sensitivity as a function of testing temperature at uniform elongation and extrapolated to zero strain.

Figure 4. Effect of cold-rolling reduction and degree of recrystallization on the temperature of minimum strain rate sensitivity.

Figure 5. Effect of grain size and strain rate on the temperature of minimum strain rate sensitivity.

Table I. Chemical composition of Zircaloy-2 strip (wt.-%)

Sn	Fe	Cr	Ni	O	C	N	H	Zr
1.46	0.109	0.092	0.050	0.136	0.006	0.002	0.002	balance

Table II. Cold-rolling reduction and degree of recrystallization in Zircaloy-2 strip. Grain size after full recrystallization, in mean linear intercept. 4 hours 400 500 600 700°C

Cold-rolling reduction	10 %	20 %	40 %	60 %	75 %	
Degree of recrystallization	0 %	0 %	0 %	0 %	10 %	400
	35 %	25 %	40 %	30 %	35 %	500
	65 %	70 %	50 %	60 %	65 %	600
	100 %	100 %	100 %	100 %	95 % 100%	700
Grain size (μm)	18	15	8.4	7.6	6.3	

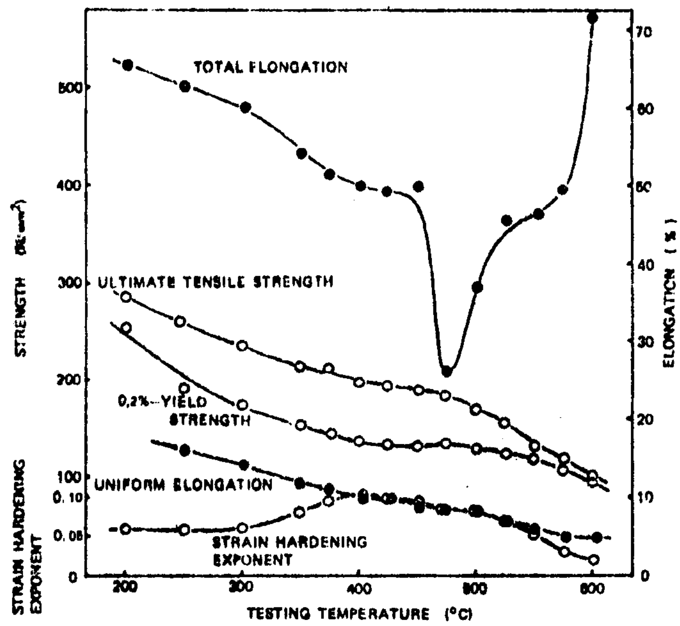

Figure 1. Strength, ductility and strain hardening in Zircaloy strip cold-rolled 60 % and fully recrystallized as a function of tensile testing temperature.

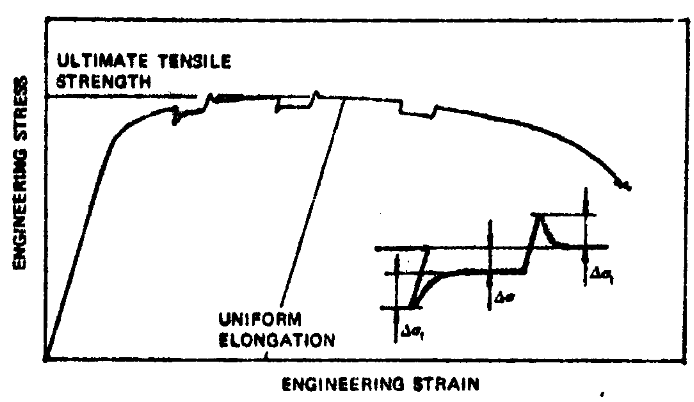

Figure 2. Engineering stress-strain curve with steps produced by strain rate reductions. Measurement of stationary and transient flow stress change.

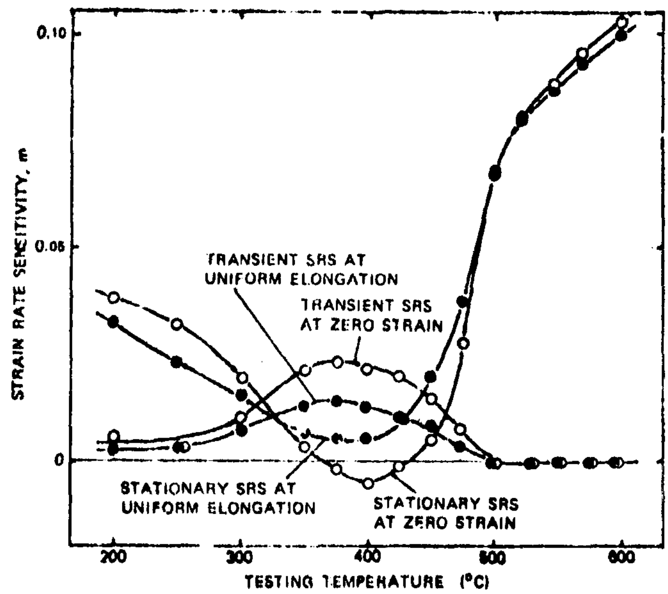

Figure 3. Stationary and transient strain rate sensitivity as a function of testing temperature at uniform elongation and extrapolated to zero strain.

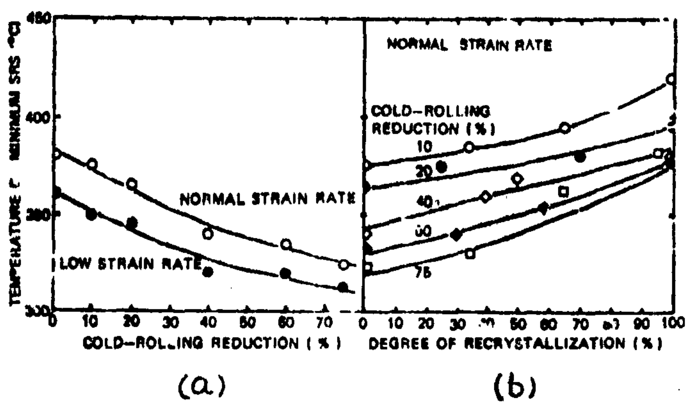

Figure 4. Effect of cold-rolling reduction and degree of recrystallization on the temperature of minimum strain rate sensitivity.

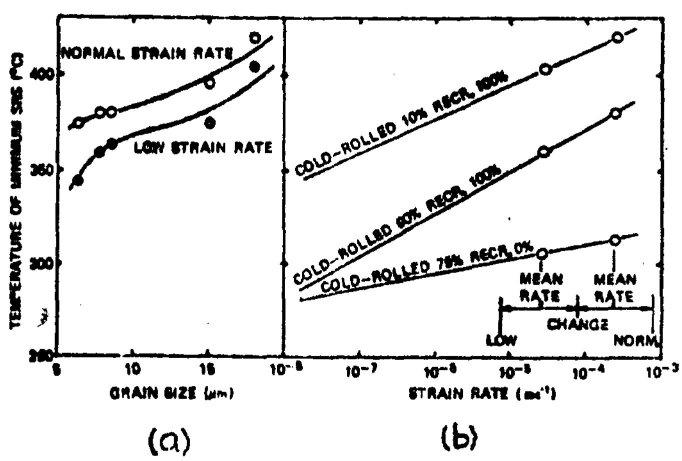

Figure 5. Effect of grain size and strain rate on the temperature of minimum strain rate sensitivity.